

Alma Mater Studiorum – Università di Bologna

DOTTORATO DI RICERCA IN SCIENZE VETERINARIE

Ciclo XXXV

Settore Concorsuale: 07/H1 ANATOMIA E FISIOLOGIA VETERINARIA

Settore Scientifico Disciplinare: VET /01 ANATOMIA DEGLI ANIMALI DOMESTICI

**Longitudinal Micro-CT driven biomarkers as a tool to evaluate lung
fibrosis progression and antifibrotic efficacy in a refined Bleomycin
mouse model**

Presentata da: *Zahra KHALAJZEYQAMI*

Coordinatore Dottorato

Prof. Carolina Castagnetti

Supervisore

Prof. Luciana Giardino

Co-supervisore

Prof. Maurizio Mazzoni

Dr. Franco Fabio Stellari

Esame finale anno 2023

Contents

Abstract	4
Introduction	5
Idiopathic Pulmonary Fibrosis.....	5
Incidence and prevalence of IPF	6
Risk factors	6
Diagnosis of IPF, staging and prognosis.....	7
Current therapies and new relevant targets for IPF	9
Murine models for IPF in Drug Discovery	10
Asbestosis	11
Fluorescein Isothiocyanate (FITC)	11
Age-related models.....	12
Cytokines overexpression	12
Amiodarone	13
Bleomycin	13
Pathogenesis of IPF	16
Epithelial-to-Mesenchymal Transition (EMT).....	17
Role of fibroblasts and myofibroblasts in IPF	18
Role of Matrix metalloproteinase.....	20
Imaging technologies.....	20
Micro-CT imaging.....	21
Aim of the study	23

Material and Methods	23
Experimental Animal	23
Optimization of BLM dose and administration scheme	24
Pharmacological validation: Nintedaninb administration	25
Micro-CT imaging	26
Analysis of CT scans	27
Bronchoalveolar lavage and cell count	30
Matrix metalloproteinases and TIMPs measurement	30
Histological staining on lung tissue sections	30
Results.....	31
Setting up the optimized murine lung fibrosis model	31
Clinical observation.....	31
Micro-CT analysis	32
Inflammatory cells infiltration count	36
Histological evaluations	38
Time course characterization of triple OA of 6µg of BLM-lung fibrosis model	40
Clinical observation.....	40
Micro-CT analysis	40
BALF: inflammatory cells	41
BALF: matrix metalloproteinases	42
Histological evaluation	43
Evaluation of antifibrotic response to Nintedanib following different therapeutic schedules	45
Clinical observation.....	45

Micro-CT.....	46
BALF: inflammatory cells count.....	47
Matrixins assessment	49
Histological evaluation	49
Discussion	50
Conclusion.....	53
Bibliography.....	55

Abstract

Idiopathic pulmonary fibrosis (IPF) is a chronic progressive disease with no curative pharmacological treatment. Animal models play an essential role to reveal molecular mechanisms involved in the pathogenesis of the disease.

Bleomycin (BLM)-induced lung fibrosis is the most widely used and characterized model for anti-fibrotic drugs' screening. However, several issues have been reported, such as the identification of an optimal BLM dose and administration scheme as well as gender-specificity. Moreover, the balance among disease resolution, an appropriate time window for therapeutic intervention and animal welfare remains critical aspects yet to be fully elucidated.

In this thesis Micro CT imaging has been used as a tool to identify the ideal BLM dose regimen to induce sustained lung fibrosis in mice as well as to assess the antifibrotic effect of Nintedanib (NINT) treatment upon this BLM administration regimen.

In order to select the optimal BLM dose scheme, C57bl/6 male mice were treated with BLM via oropharyngeal aspiration (OA), following either double or triple BLM administration.

The triple BLM administration resulted the most promising scheme, able to balance disease resolution, appropriate time-window for therapeutic intervention and animal welfare.

The fibrosis progression was longitudinally assessed by micro-CT every 7 days for 5weeks after BLM administration and 5 animals were sacrificed at each timepoint for the BALF and histological evaluation. The antifibrotic effect of NINT was assessed following different treatment regimens on this model.

Herein, we have developed an optimized mouse model of pulmonary fibrosis, enabling three weeks of therapeutic window for the screening of putative anti-fibrotic drugs. micro-CT scanning, allowed us to monitor the progression of lung fibrosis and the therapeutical response longitudinally in the same subject, drastically reducing the number of animals involved in the experiment.

Introduction

Idiopathic Pulmonary Fibrosis

The American Thoracic Society and the European Respiratory Society (ATS and ERS) introduced Idiopathic Pulmonary fibrosis (IPF) as a chronic, progressive form of fibrosing interstitial pneumonia with the histopathological pattern of usual interstitial pneumonia (UIP) with an unknown cause [1], [2].

IPF occurred in adults typically after age 50 and commonly manifests an unexplained chronic exertional dyspnea, cough, bibasilar inspiratory crackles and finger cobbling. Most patients manifest a slow, gradual decline of respiratory functions until eventual death from respiratory complications in 2-3 years, but some patients may experience acute respiratory worsening with other comorbid conditions such as emphysema and pulmonary hypertension and lung cancer which could affect drastically the quality of life and life expectancy [3].

This disease mainly occurs in elderly men (typically 60-70 aged) rather than women, and most of them have a history of cigarette smoking [4]. IPF is limited to the lungs and is associated with the histopathologic and/or radiologic pattern of Usual Interstitial Pneumonia (UIP). The histopathological hallmark of UIP is the presence of heterogeneous areas severely affected by fibrosis, especially subpleural and paraseptal regions, alternated with areas of less affected or normal parenchyma [2], [3].

Most severe regions are characterized by inflammatory infiltrate, mainly composed of lymphocytes, and fibrotic zones with dense collagen and proliferating fibroblasts and myofibroblasts "*fibroblast foci*". The most accredited hypothesis which leads to the development and sustainability of the fibrotic cascade involves repeated micro-injuries of the alveolar epithelium at first and an altered repair process [5]. These result in aberrant epithelial-fibroblast communication with an accumulation of myofibroblasts, the master producers of extracellular matrix, followed by the remodeling of lung parenchyma. In the advanced stage of fibrosis, lung architecture is completely altered, and the

alveoli are replaced by large air spaces, defined as honeycomb lungs, with thick fibrotic walls lined by bronchiolar epithelium and often filled with mucin and inflammatory cells. These morphological alterations of lung tissue leading to decreased lung compliance disrupted gas exchange, and ultimately respiratory failure and death. Over 80 % of all reported fatalities in IPF patients are due to respiratory failure, even though, heart failure, bronchogenic carcinoma, ischemic heart disease, infection and pulmonary embolism are also other causes of mortality [6].

Incidence and prevalence of IPF

IPF is the most common form of idiopathic interstitial pneumonia (IIP) among over 150 known forms of ILD [7]. IPF is generally identified in the middle-aged (between 40 and 70 years of age) with higher incidence in men than in women [5]. Incidence and prevalence of IPF are influenced by geographic, ethnic, cultural or racial factors and the enrolled populations and trial designs are not consistent. However, according to recent epidemiologic studies conducted in the first years of the 2000s in the USA the prevalence of IPF was estimated between 14 and 42.7 per 100,000 population, with a higher rate for men and an incidence rate between 6.8 and 16.3 per 100,000 persons [4]. Some population-based study suggests that the number of new IPF cases is projected to increase over time and that the number of new cases in the USA will become 12,000-21,000 by 2050 [8].

Risk factors

Despite the unknown aetiology of IPF, the role of multiple genetic mutations and environmental risk factors have been confirmed. The most described include:

- cigarette smoking (history of more than 20 pack-years) [8]
- environmental exposures especially to metals (brass, lead and steel) or wood dust (pine) and farming [9].
- chronic viral infections, i.e. Epstein-Barr virus [10], Human cytomegalovirus [11] and Hepatitis C virus[12];

- gastro-esophageal reflux, is often associated with acid micro-aspiration that may be linked to repetitive injuries in the lung epithelium [13].

Up to 5% of total patients with IPF are affected by familiar forms of IPF suggesting a potential involvement of some genetic factors. Familial IPF is often associated with a mutation in genes for surfactant proteins C (SPC) and A2 (SPA2) and with genetic variants within the telomerase-related genes (TERT and TERC) and Mucin 5B (MUC5B) gene [5]. Regardless of the many conducted studies, the detailed role of each risk factor in IPF has not yet been confirmed, suggesting the multifactorial nature of IPF.

Diagnosis of IPF, staging and prognosis

The ATS/ESR with the American college of chest physicians (ACCP) in 2000 provided specific guidelines regarding the diagnosis and management of IPF (ATS and ERS 2000). Later, in 2012 [5] a new statement relied on recent studies and suggested the following requirements to diagnose IPF:

1. Exclusion of any other known causes of ILD like; domestic and environmental exposures, connective tissue diseases or any drug toxicities.
2. Confirming the presence of UIP pattern by high-resolution computed tomography (HRCT)

The application of HRCT increased drastically the level of confidence in the diagnosis of IPF. HRCT could differentiate IPF from other forms of UIP thanks to a detailed evaluation of lung parenchyma [14].

A typical UIP pattern is sufficient to secure a diagnosis of UIP/IPF without the need to perform a surgical lung biopsy or another invasive testing [14]. It is characterized by the presence of obligatory reticular opacities, often associated with traction bronchiectasis, subpleural honeycombing (**Figure 1A-B**), which appears as clustered cystic airspaces (usually with diameters of 3-10 mm), ground glass opacities and fibroblast foci.

The distribution of UIP on HRCT is usually basal and peripheral, and often patchy. The presence of other abnormalities (e.g., calcifications, pleural effusion), however, suggests a different aetiology for UIP pattern.

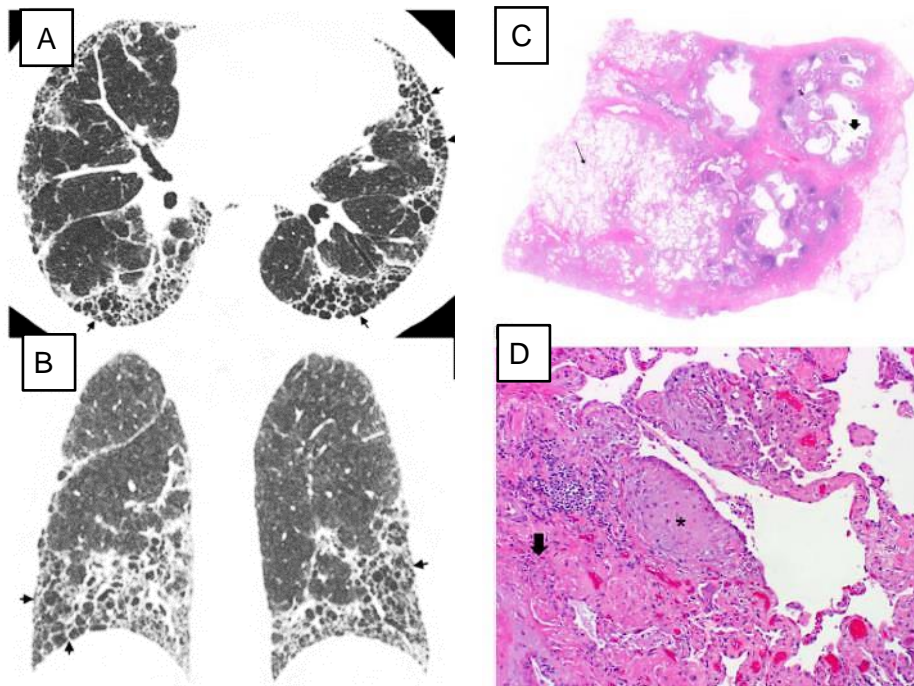


Figure 1: High-resolution computed tomography (HRCT) scans reveal UIP pattern with extensive honeycombing (*arrows*). A: axial view and B: coronal view. A surgical lung biopsy specimen evidences UIP pattern, showing (C) patchy honeycombing (*thick arrows*) and some “normal” lung regions (*thin arrows*), and in (D) more severe fibrotic regions (*thick arrows*) closed to a fibroblast focus (*asterisk*). This figure has been adapted from Raghu et al. (2011) (Raghu et al. 2011).

In case of suspected UIP, additional investigations, including surgical lung biopsy, should be considered, to confirm the presence of a UIP histological pattern (**Figure 1C-D**). Accordingly, an interdisciplinary discussion between pulmonologists, radiologists and pathologists is still necessary to evaluate the various features, stages and treatment protocols, and despite this, a small number of patients still remains unclassifiable [5].

The experts have suggested the terms mild, moderate, severe, early and advanced for staging the IPF. These nominations are designated based on pulmonary function tests and High-Resolution

Computed Tomography (HRCT) abnormalities, which is important to predict the risk of mortality within 2 years and consider lung transplantation [5].

Current therapies and new relevant targets for IPF

There is no pharmacological treatment for IPF with high outweighed desirable effects over its adverse effects [15], [16]. Two tyrosine kinase inhibitors, nintedanib (NINT) and pirfenidone, have been approved by the US Food and Drug Administration (US FDA) for the treatment of IPF, due to their safety and efficacy in decelerating of functional decline and disease progression, in agreement with the recommendations of the ATS and ERS guidelines [4], [17]. In particular, pirfenidone is an oral drug either with anti-inflammatory, antifibrotic or antioxidant effects; it was selected for the treatment of patients with mild to moderate pulmonary fibrosis under certain conditions, and it was approved as therapy in Europe in 2011 [17]. Nintedanib, instead, is a potent small molecule which inhibits the receptor of tyrosine kinases PDGF receptor, FGF receptor and vascular endothelial growth factor receptor [18] that could decelerate the development and progression of lung fibrosis. Despite, lack of certain treatments for IPF, these drugs have been shown to hinder the progression of IPF in case of early administration, without any impact on the mortality rate [16]. The in vitro studies have been shown the inhibitory effect of NINT on PDGF-BB, bFGF and VEGF on primary human lung fibroblast [19], moreover some studies have been demonstrated the role of NINT in attenuation of some profibrotic mediators [20]. NINT has shown anti-fibrotic and anti-inflammatory effects on animal models of lung fibrosis [21], [22].

In some cases, oxygen supplementation is suggested but, no survival benefits were found after long-term oxygen therapy. Lung transplantation remains the most effective therapy for IPF patients. This option is highly recommended in patients with poor prognosis (less than 2 years) but there is no clear data to address the clinicians toward this decision. Lung transplantation can increase the survival rates by 50%-56% after 5 years of surgery [13], [23].

Murine models for IPF in Drug Discovery

Animal models are essential to understand the pathobiology of human diseases such as pulmonary fibrosis, for the validation of new therapeutic targets and for the selection of the best drug candidates in drug discovery [23], [24].

For IPF, it has been reported a great number of different animal models with their particular features; however, none of them fully recapitulates the histologic pattern of the human lung disease or exhibits characteristics of the progressive and irreversible disease [25]. This discrepancy between preclinical and clinical features aggravates the difficulty of validating new drug compounds in preclinical research: Among several significantly effective anti-fibrotic compounds in animal models, only a few of them could reach hardly in clinical trials. Thus, there is an urgent need to develop animal models that strictly mimic the features of human disease and standardize their use for preclinical drug efficacy studies, to select promising drug candidates [26].

Although it is recognized that the spontaneous development of lung fibrosis in domestic animals (cats, dogs, etc.) can be informative, the recently published guidelines recommend the use of mice as first line animal model for drug testing, despite they do not fully replicate classical IPF histopathology, probably explained by anatomic differences between murine and human lungs, temporal homogeneity of animal models and potentially distinctive pathobiological mechanisms involved in human disease. Rats, instead, can be used as a second species for other considerations, if required [27].

Despite IPF is a disease affecting the elderly population, most preclinical studies utilize mice aged 6-8 weeks [26]. Although some studies proved that aged mice can better reflect human pulmonary fibrosis [26], [28].

The most used approaches to provoke pulmonary fibrosis in mice are based on the use of etiological agents, which can generate the first damaging insult triggering the fibrotic process in the lung. Some of these agents include X-ray radiation [29], fluorescein isothiocyanate (FITC), asbestos and silica, fibrinogenic cytokines (e.g. TGF β and interleukins) [30], transgenic mice or gene transfer including

fibrogenic mediators [31] and bleomycin[27], oxidants and phorbol myristate acetate (PMA)[30]. Besides these agents, it has been reported that virus infection can induce fibrosis progression in humans and animals (e.g. γ -herpesvirus in mice and horses) [26]. For this reason, other approaches to induce lung fibrosis in mice were based on the use of viral vectors (i.e. adenovirus and lentivirus) delivering profibrotic transgenes directly into the lung[27], [32].

However, the most currently used and well-characterized model for IPF is the bleomycin-induced model. Since different strains can have varied susceptibility to develop fibrosis following bleomycin administration, C57BL/6J mice were found to be a strong responder to bleomycin compared to BALB/c mice which are relatively resistant to fibrosis, probably due to higher expression of the enzyme bleomycin hydrolase in BALB/c rather than C57BL/6J mice [25], [33]. Here, we focused on some animal models of lung fibrosis.

Asbestosis

This model was established by single intrathecal or inhalation administration of asbestos fibers. Asbestos-induced lung fibrosis is distinguishable from IPF by histological findings like asbestos bodies within the fibrotic tissue, the intratracheal administration induced an unevenly distributed fibrosis in central areas of the lungs rather than subpleural which occurred following the inhalation administration. The deposition of asbestos fibers initiates fibrosis by overproduction of profibrotic cytokines, alveolar epithelial apoptosis, and M2 polarization of macrophages which lead to ECM production and deposition [34], [35]

Fluorescein Isothiocyanate (FITC)

In this model, the fibrosis is located within the area of FITC deposition and can be obtained via intratracheal administration of 0.007mg per gram body weight of FITC. The advantage of this model is robustness and long-lasting fibrosis in both Balb/c and C57bl/6 for a month. The fibrosis occurs following acute injury, oedema and inflammation via recruitment of neutrophils and activation of Th2 and production of its cytokine (IL-13). The size of FITC particles and the freshness of the FITC solution could affect the reproducibility of this model [36].

Age-related models

Recent studies have shown old mice are more sensitive to BLM than young mice. The transgenic mice with deletion of the receptor of advanced glycation and products (RAGE^{-/-} mice)[37] or Ralxin (relaxin^{-/-} mice) develop lung fibrosis spontaneously. And this progression is more evident in male mice than in female mice [38]. Moreover, the infection of old mice with γ -herpesvirus-68 also leads to lung fibrosis as a consequence of epithelial cell endoplasmic reticulum stress and upregulation of TGF- β [39].

Many cellular responses involved in fibrosis are active in old mice; Besides the upregulation of matrix metalloproteinase-9 in aged mice, the decrease of thymocyte differentiation antigen 1 (Thy-1) which is known as a hallmark of human myofibroblast and molecular association with TGF- β activation in myofibroblast intrigue scientist to use the aged mice to establish the lung fibrosis models [40], [41].

Cytokines overexpression

The overexpression of some cytokines, like TGF- β , TGF- α , IL-13, TNF- α , and IL-1 β via a transgenic or gene-transfer approach could cause lung fibrosis. Doxycycline-regulated transgenic expression in epithelial cells [42]and adenoviral-mediated TGF-overexpression [32] increase the TGF- β in the lungs which may mimic the IPF in a later stage, additionally, epithelial cell apoptosis and variation in soluble mediators lead to persistent scarring due to collagen deposition and depict fibrosis in human. Moreover, the C57bl/6 strain has shown more response to TGF- β compared to Balb/c [27].

The overexpression of IL-13 could also be achieved by a transgenic approach. The IL-13 transgenic mice develop both airway and parenchymal fibrosis [43] although the lung scarring is mediated by TGF- β activity to regulate the profibrotic effect of IL-13. Adenoviral-mediated IL1 β was also used to induce lung fibrosis and an increase in α -smooth muscle actin (α -SMA)-positive cells at day 14 and an increase in lung collagen from day 21 to 60. Over expression of IL-1 β , increase also the concentration of TGF- β and PDGF in the lung [27].

The TNF- α gene transfer via adenoviral vector has been used to establish lung fibrosis. TNF- α results in an early inflammation by activation of neutrophils, macrophages and lymphocytes which might cause α -SMA positive cells from day 7-14. Due to the complex role of TNF- α in promoting and inhibiting lung fibrosis, this model remains debatable [44].

Amiodarone

Amiodarone (AM) is a bi-iodinated benzofuran, widely used as an antiarrhythmic agent. Amiodarone-related adverse pulmonary effects continue to be observed in 10-17% and with fatalities in about 10% of patients who received AM.

AM toxicity includes several distinct features from inflammatory reactions like eosinophilic pneumonia and nonspecific interstitial pneumonia-like idiopathic pulmonary fibrosis-like interstitial pneumonia. Age of patients, duration and dosage of AM are considered the significant risk factors to develop lung toxicity [45].

AM has been administered via intratracheal or aerosol in different dosages to establish lung fibrosis in C57bl/6, F344 rats and hamsters [46]–[48]. All the studies have shown mild to moderate lung fibrosis for 3 weeks as a result of the inflammatory response, Epithelial cells apoptosis and necrosis [49]. The administration of AM in Kunming mice [50] has shown interstitial fibrosis, the thickness of alveolar septa, type 2 cell hyperplasia and accumulation of foamy alveolar macrophage.

Bleomycin

Bleomycin (BLM) is a complex glycopeptide, isolated from a strain of actinobacteria “*Streptomyces verticillus*” and is used for human cancer therapy [51]. BLM is an antineoplastic drug which is used for various carcinoma and lymphoma and induces toxicity in the lung, skin and mucous membrane because of the lack of Bleomycin hydrolase in those tissues [52], [53]. Lung fibrosis is known as a consequence of BLM administration in 3-5% of patients receiving this agent. This agent seems to cause lung damage through direct DNA strand breakage, interrupting the cell cycle and leading to apoptosis and inducing oxidative stress [54], [55]. The consequent inflammatory response causes

pulmonary toxicity, fibroblast activation, and finally the development of fibrosis. However, the BLM doses used in the preclinical studies might not cause significant DNA damage [56]. For this reason, bleomycin has been used such an inducer of pulmonary fibrosis in a wide variety of experimental animals including mice, rats, hamsters, rabbits, guinea pigs, dogs, and non-human primates [27]. Its side effect has been used to establish animal models of lung fibrosis. For the first time, BLM was used in dogs and then mice, hamsters, rats and sheep. The BLM-induced lung fibrosis in murine is the most-used model to study the molecular mechanism underlying IPF, identify the new therapeutic targets and subsequently for drug discovery.

Despite, the limitations of this model to mimic the human chronic progressive lung fibrosis, the BLM model has been used vastly for drug discovery. Besides its many advantages like the easy induction and high reproducibility, shares also many disadvantages like the auto resolution after 2 weeks which is shorten the therapeutic windows and limits the assessment of the efficiency and toxicity of antifibrotic compounds.

Route of delivery and Dose regimen

Single intratracheal administration of BLM is mostly used method to induce lung fibrosis. Although some studies have suggested that repetitive i.t administration with a lower dose leads toward sustainable fibrosis to depict the chronic aspects of lung fibrosis[25].

Systemic delivery of BLM via osmotic mini pump or intravenous also have been considered in several studies [22], [57]. The oropharyngeal administration of BLM has been shown by as an easy and fast route for developing homogenously-distributed fibrosis in mice [21], [58].

A wide range of BLM based on animal weight and protocol is reported. The commonly used doses through direct i.t are 2 U/kg in C57BL/6, 10 U/kg in BALB/C and 7.5 U/kg in Fisher 344 rat. Mortality is a positive correlation with higher doses and usually occurs in the acute phase and before the establishment of fibrosis [21], [22], [36], [59].

Strain, Age, Gender

C57BL/6 mice respond highly to BLM, whereas DBA/2 mice are less susceptible and BALB/C mice are resistant to BLM and don't develop lung fibrosis. This effect is not clearly explained but it might

depend on the expression levels of Bleomycin hydrolase, as well as the cytokines and other enzymes production[60]. Recent studies have highlighted the higher susceptibility of male mice compared to female mice[61].

IPF is shown a tendency as a male predominance disease. The AST and NIH suggest the use of both males and female in preclinical research to provide more relevant translational information.

Sequence of events in BLM-induced Lung fibrosis and pharmacological intervention

Single intratracheal administration of BLM is used mostly to induce fibrosis. BLM-induced lung fibrosis is characterized by a period of acute lung inflammation within the first week after bleomycin administration, followed by a fibro-proliferative phase with a peak at day 14 and a fibrotic phase (up to 21 days) which usually resolves in a variable time [62], [63]. It is important to distinguish between the inflammatory and fibrosis phase to establish the proper pharmaceutical intervention. The anti-inflammatory compound should be administered during the early phase before day 7 and it could be considered a preventive therapy. On another hand the antifibrotic substances might be more effective during the establishment of the fibrotic phase (Fig.2), thus, the 2 weeks treatment with antifibrotic compounds might not fully demonstrate their efficacy and toxicity [64], [65].

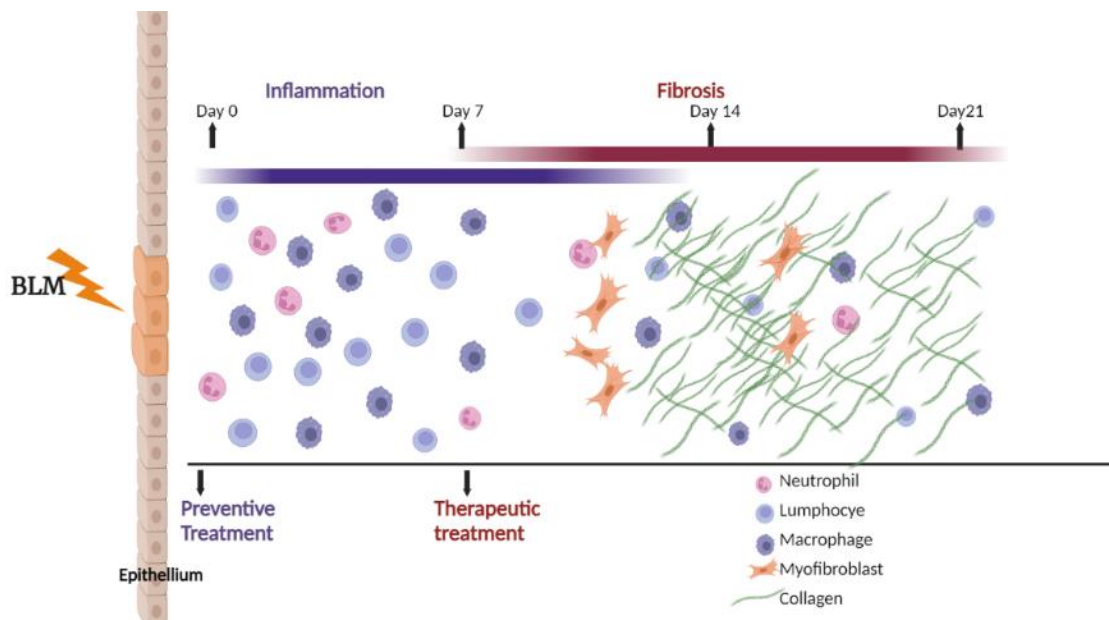


Figure 2: Illustration of event sequences after a single administration of BLM in the lung with the appropriate times for pharmacological interventions. -created with [BioRender.com](https://www.biorender.com).

BLM-lung fibrosis model limitations

BLM-induced lung fibrosis shares several valuable histological and morphological hallmarks of lung fibrosis in humans. However, despite the successful efficacy results of the anti-fibrotic compound, just a few of them are translated into clinical therapies [26], indicating the potential limitation of this model. BLM model unlike the progressive and irreversible fibrosis in IPF patients represents self-limiting and temporal fibrosis. The absence of fibroblast foci in BLM-model as an important hallmark of IPF could affect the assessment of the efficacy of some compounds [5]. In addition, BLM alters experimental drug efflux by upregulation of specific transporters which can reduce the exposure of experimental compounds to the lungs and interferes with the efficacy of these compounds [66]. Another important limitation of this model is the presence of acute inflammatory response following BLM administration. An improper therapeutic window might restrict the effect of antifibrotic compounds and increase mortality in preclinical studies [67].

Pathogenesis of IPF

The pathogenesis of IPF is multi-factorial and not yet fully understood. The current and accepted hypothesis suggests that IPF is the result of recurrent micro-injuries at the alveolar epithelial cells (AECs). The induction of aberrant and non-resolving wound-healing response leads to abnormal epithelial-mesenchymal interactions. A fibroblast-activated process of reactivation of signalling pathways also induces the secretion of pro-inflammatory molecules which activate fibroblasts proliferation and excessive deposition of collagen and extracellular matrix (ECM) components by myofibroblasts [68], [69]. All these aberrant mechanisms generate a progressive malformation of lung architecture, increase lung rigidity and thickening of alveolar-capillary barrier thus associated with a decrease in alveolar gas exchange and loss of lung function [4], [69], [70]. The whole pathogenic cascade involves a multitude of cell types, including alveolar macrophages, epithelial cells, inflammatory cells, fibroblasts and myofibroblasts, which produce and release pro-fibrotic mediators involved in epithelial cell injury and apoptosis, and furthermore in fibroblast recruitment and activation. Overall, the process of the abnormal wound healing model of IPF is reported in Figure 3.

Epithelial-to-Mesenchymal Transition (EMT)

The primary gas-exchanging interface of the lungs, which allows diffusion of oxygen and carbon dioxide between alveolar airspace and blood, is composed of 2 types of monolayers of alveolar epithelial cells (AECs) and endothelial cells, separated by their basal membranes.

AECs type I have a flat morphology and they cover 95%–98% of the alveolar-capillary interface, where they are highly specialized in gas exchange regulation. AECs type II, instead, have a cuboidal morphology and they are the progenitor cells with a crucial role in the regeneration of AECs type I and II during lung homeostasis or after injuries [71].

In normal conditions, AECs type II undergo hyperplastic proliferation and trans-differentiation into AECs type I to repair the basal membrane after injury. In IPF lungs, hypertrophic AECs type II remain in the lungs without trans-differentiate and together with inflammatory cells, secrete several fibrogenic growth factors, including platelet-derived growth factor (PDGF), tumour necrosis factor- α (TNF- α) and transforming growth factor- β (TGF- β) [72], [73], creating a profibrotic environment with an aberrant tissue-repair response. These growth factors, especially TGF- β , are involved in perpetuating injury and apoptosis of AECs, as well as inducing activation, invasion, and apoptosis resistance of fibroblasts. This phenomenon has been named the “apoptosis paradox” and although mechanisms through which this microenvironment causes programmed death of a cellular type (AECs) and proliferation of another (fibroblasts and mesenchymal cells) need to be further elucidated, it probably derives from different post-receptor signalling mechanisms [74]–[76].

In this scenario, EMT is a process in which the AECs type I lose their differentiation in epithelial cells, by downregulating the expression of E-cadherin and other proteins that form cell junction complexes, and they become cells of the mesenchymal lineages, showing a reduced cell adhesion and increased motility and expressing mesenchymal markers, such as fibronectin and α -smooth muscle actin (α -SMA), and other proteins characteristic of the mesenchymal cell-cell interactions (N-cadherin). Such interactions are weaker than the junctions of the epithelial cells and facilitate migration and invasion [77]. In physiologic conditions, EMT is a reversible event necessary for

embryonic development but it becomes dysregulated during a response to injury, fibrosis and carcinogenesis. During fibrosis, the persistence of signals produced by the EMT process generates an accumulation of extracellular matrix (ECM) causing lung tissue remodelling and organ dysfunction [73].

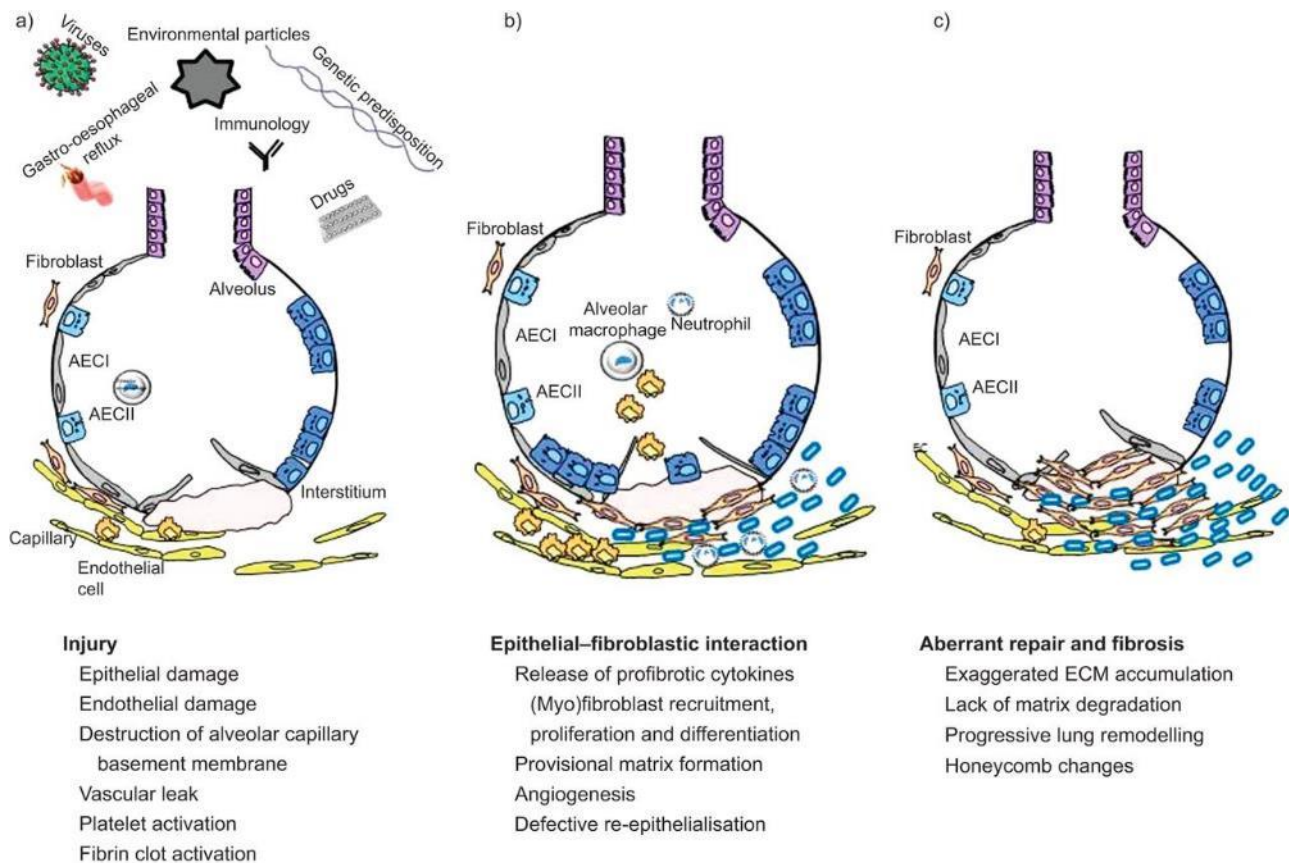


Figure 3: Representative scheme of the most relevant elements involved in the induction and progression of fibrosis. This figure has been adapted from Wuyts et al. (2013) (Wuyts et al. 2013).

Role of fibroblasts and myofibroblasts in IPF

Fibroblasts are spindle-shaped and not terminally differentiated mesenchymal cells, characterized by various functions and plasticity [78]. They play a key role in producing and secreting proteins that compose the ECM, such as collagen and fibronectin, as well as glycosaminoglycans and proteoglycans that constitute the space-filling elements of the connective tissue. Fibroblasts also regulate the turnover of the matrix through the expression of matrix metalloproteinases (MMPs),

which degrade the ECM, and their inhibitors, tissue inhibitors of metalloproteinases (TIMPs), and participate in the wound healing process and the regeneration of the damaged tissue.

In IPF, the normal epithelial-mesenchymal crosstalk is disrupted due to AECs type II, which acquire a profibrotic phenotype followed by an aberrant secretion of profibrotic mediators as paracrine factors, like TGF β and CTGF that stimulate and activate differentiation of fibroblasts into a myofibroblast phenotype. Myofibroblasts assume features, such as the augmented expression of α -SMA, contractility, the greater rate in the synthesis and secretion of ECM and resistance to apoptosis [78], [79] either common to fibroblasts or to smooth muscle cells, and are responsible for the abundant synthesis of matrix and collagen in ECM, as observed in pulmonary fibrosis. This excess of ECM deposition alters the integrity of the surrounding parenchyma and causes further epithelial cell death.

In IPF, active fibroblasts and myofibroblasts are organized in clusters named *fibroblastic foci*, which are recognized as histological hallmarks of lung fibrosis [4], [80]. They are generally closed to alveolar regions of hyperplastic or apoptotic epithelial cells, strengthening the proposed role of AECs in fibroblast transformation. Activated fibroblasts are induced to produce huge quantities of components of the ECM and some of them, i.e. elastin, collagen type V, and tenascin C contribute to establishing a positive feedback mechanism, stimulating the continuous cellular differentiation into myofibroblasts [81].

The origin of fibroblasts and myofibroblasts and their organization in foci in IPF is still unclear; it has been established that although the resident fibroblasts are the predominant source, during tissue remodelling and fibrosis, myofibroblasts can origin also from other cell types, such as AECs that have undergone the EMT and fibrocytes, which are mesenchymal progenitors that exhibit mixed morphological and molecular characteristics of hematopoietic stem cells monocytes and fibroblasts, present in the systemic circulation. Strong evidence indicates that AECs are the primary source of mediators that function as chemotactic factors or mitogens for mesenchymal cells, including PDGF, TGF- β , TNF- α , and endothelin 1 [72]. These factors probably contribute most to the migration, proliferation, and differentiation of resident mesenchymal cells.

Role of Matrix metalloproteinase

Aberrant alveolar epithelial cells activation, fibroblast proliferation and transition to myofibroblast are affected by numerous mediators which exaggerate the accumulation of extracellular matrix (ECM) and alter the lung architecture. Matrix metalloproteinases (MMPs) are among these mediators. MMPs are zinc-dependent endopeptidases that besides the enzymatic effect in the degradation of ECM components, they cleave and activate growth factors, cytokines and chemokines [82], [83]. MMPs dysregulation has been indicated as a central player in abnormal tissue remodelling in IPF patients as well as in animal models [84]. MMPs are classified into different groups by their substrate and their roles are still under investigation; MMP-2 and -9 are known as gelatinases and degrade the collagen and basement membrane proteins, and are expressed by epithelial cells, macrophages, lung fibroblasts and endothelial cells. Its higher expression is found in IPF patients close to fibrotic foci and is found in the lungs of experimental mice [83], [85]. MMP -1 and -8 cleave type I interstitial collagen and may increase the pulmonary fibrosis features by cleavage of IL-10 in the murine models [86]. MMP-12 is a metalloelastase expressed by macrophages and lung stromal cells and is found in lung and serum of patients with interstitial lung disease and systemic sclerosis, some studies reported its role in promoting fibrosis in murine lungs by antibody-mediated cluster of differentiation 95 (CD95) or apoptosis antigen-1 (FAS) activation [83], [87], [88]. The four members of the tissue inhibitor of metalloproteinases (TIMPs) are endogenous inhibitors of MMPs and are needed to better understand in a context of lung fibrosis. TIMP-1 was found in interstitial macrophages and might regulate MMP-8 and 13 besides the pro-MMP-9 activating cleavage [89], [90] and TIMP-2 was found in fibroblast foci, the studies have been demonstrated the correlation of TIMP-4 with inflammation and fibrosis [91]. There are still many unknown aspects of MMPs and their involvement in IPF to learn.

Imaging technologies

In the last decades, imaging technologies have become an interesting tool in preclinical research and in drug development studies, providing the opportunity for investigating cellular and molecular pathways and *in vivo* mechanisms of disease in a living organism in real-time. Since they include

non-invasive technologies, animals can be subjected to multiple imaging sessions during the experiment becoming their own controls during the experiment. This allows to considerably reduce the number of animals required per experiment, fully in compliance with the ethical “3R” principle (replacement, reduction, refinement) [92] and to decrease either the intra-experiment or the inter-experiment variability.

The most common and suitable imaging technologies used for *in vivo* small-animal imaging are optical images, such as Bioluminescence Imaging (BLI) and Fluorescence Molecular Tomography (FMT), computed tomography (CT), magnetic resonance imaging (MRI), and finally methods of nuclear medicine: positron emission tomography (PET) and single photon emission computed tomography (SPECT).

In particular, in this work, we mainly used micro-CT imaging for the observation of anatomical modifications in lung parenchyma and the assessment of fibrosis.

Micro-CT imaging

Micron-scale Computed tomography (micro-CT) imaging is the preclinical equivalent of clinical CT. micro-CT is known as a non-invasive three-dimensional (3-D) imaging modality providing high spatial resolution. The development of a new x-ray detector and an increasing interest in disease animal models make a micro-CT as a sophisticated and important tool for both *in vivo* and *ex vivo* imaging in preclinical studies [93]. The instrument is composed of an X-ray source and a detector, which are mounted on a rotating gantry while the animal lies on a bed support during acquisition. Scanners for *in vivo* applications on live animals (mostly mice and rats) are equipped with tubes for gas administration to ensure the maintenance of anesthesia during the acquisition, since sedation cannot be avoided during *in vivo* procedures. The key component of u-CT is x-ray detector performance technology can provide a valuable anatomical and functional information in high resolution (voxel size $\leq 100\mu\text{m}^3$). The short time of scanning and a low radiation dose exposure would allow to perform a longitudinal study by reducing drastically the number of animals involved in experiments following the 3R rules scan is a useful diagnostic tool for detecting diseases and injuries. It uses a series of

X-rays and a computer to produce a 3D image of soft tissues and bones [93], [94]. It is a non-invasive technology with a wide range of applications providing high-resolution anatomical images of small animals. In lung imaging, for example, it allows the longitudinal quantification of air and tissue content, starting from X-ray attenuation through lung parenchyma. This permits to highlight parenchymal changes during a progressive disease, like lung fibrosis, or to study lung development mechanisms [21], [22], [58], [95].

The instrument is composed of an X-ray source and a detector, which are mounted on a rotating gantry while the animal lies on a bed support during acquisition. Scanners for *in vivo* applications on live animals (mostly mice and rats) are equipped with tubes for gas administration to ensure the maintenance of anesthesia during the acquisition, since sedation cannot be avoided during *in vivo* procedures [62], [94].

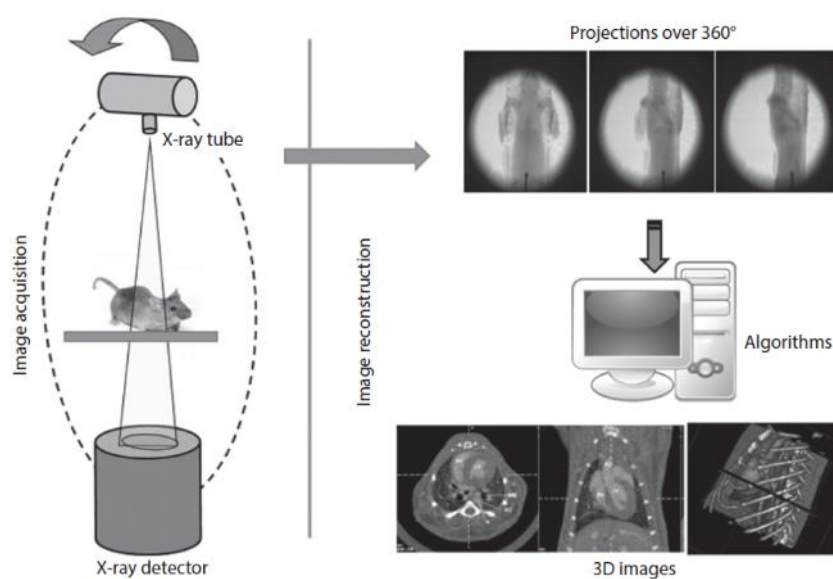


Figure 4: *micro-CT workflow: acquisition and reconstruction phases* *micro-CT workflow: acquisition and reconstruction phases (Russo and Badea 2019)*

During acquisition, many 2D projections are registered from multiple angles covering 360° of rotation, finally producing three-dimensional (3D) tomographic data at microscopic resolution (voxel size $\leq 100 \mu\text{m}^3$) [94], consisting in a 3D matrix of voxels with values proportional to the mean linear attenuation coefficient of the material within each voxel (Figure 4). The use of a respiratory gating technique, moreover, permits the reconstruction of two distinctive datasets corresponding to the

main respiratory phases (end-inspiration and end-expiration) with a better quality because less affected by motion-related artefacts [96].

The analysis of CT scans in longitudinal experiments provides important information about remodeling of lung parenchyma, through the quantification of preclinical aeration compartments defined by Mecozzi et al[62] in the end-expiratory dataset, and the assessment of functional parameters by the analysis of both respiratory phases (i.e. tidal volume, which is the volume of air ventilated into the lung during a breath) [95].

Aim of the study

Our main objective was the refinement and set up of an optimized Bleomycin-induced lung fibrosis model in C57Bl/6 male mice, to obtain a sustained pulmonary fibrosis up to 28 days for primary drug screening.

As a second goal we intended to demonstrate the capability of lung function parameters derived from longitudinal micro-CT to describe lung fibrosis progression and response to antifibrotic treatment, by comparing two and three weeks of NINT administration. (FDA approved drug for IPF treatment).

Material and Methods

Experimental Animal

All studies were performed on 7-8-week-old male C57Bl/6 mice (Envigo, san Pietro al Natisone, Udine, Italy). Animals were housed five per cage and acclimated upon arrival to the local vivarium condition (room temperature: 20–24°C; relative humidity: 40–70%; 12-h light-dark cycle; food and

water ad libitum) for 7–10 days. All Animals were kept under standard conditions at our animal facility, in compliance with the procedures and principles outlined in the European Directive 2010/63 UE, Italian D.Lgs 26/2014 and the revised “Guide for the Care and Use of Laboratory Animals” (National Research Council Committee, US, 2011). All animal procedures were conducted in an AAALAC (Association for Assessment and Accreditation for Laboratory Animal Care) certified facility at Chiesi Farmaceutici and were authorized by the Italian Ministry of Health with protocol number 841/2019-PR and by the internal AWB (Animal Welfare Body). The proper actions were taken into the consideration to minimize pain or discomfort in the animals; the pain was evaluated daily through a Visual Analogue Scale (VAS) ranging from 0 to 10 by a designated veterinarian or trained technicians. Signs of dyspnea, body weight loss $\geq 20\%$ and VAS ≥ 6 were considered as humane endpoints.

Optimization of BLM dose and administration scheme

Bleomycin hydrochloride (Baxter) diluted in final volume of 50 μ l saline. Animals were anesthetized with 2.5% isoflurane and placed on an intubation stand and the liquid was drained into the distal part of the oropharynx with a micropipette [21], [58], [97]. Male mice of 25 ± 1 gr was placed on an intubation stand and the liquid was drained into the distal part of the oropharynx with a micropipette. 30 mice (5 per group) were randomized to receive double administration with 10 or 15 μ g BLM at each shot corresponding to (0.4 and 0.6 mg/kg), whereas those receiving triple administration were given 5, 6 or 7.5 μ g BLM at each OA corresponding to (0.2, 0.25 and 0.3 mg/kg). The vehicle group

received 50 μ L saline at each administration. A schematic representation of the experimental

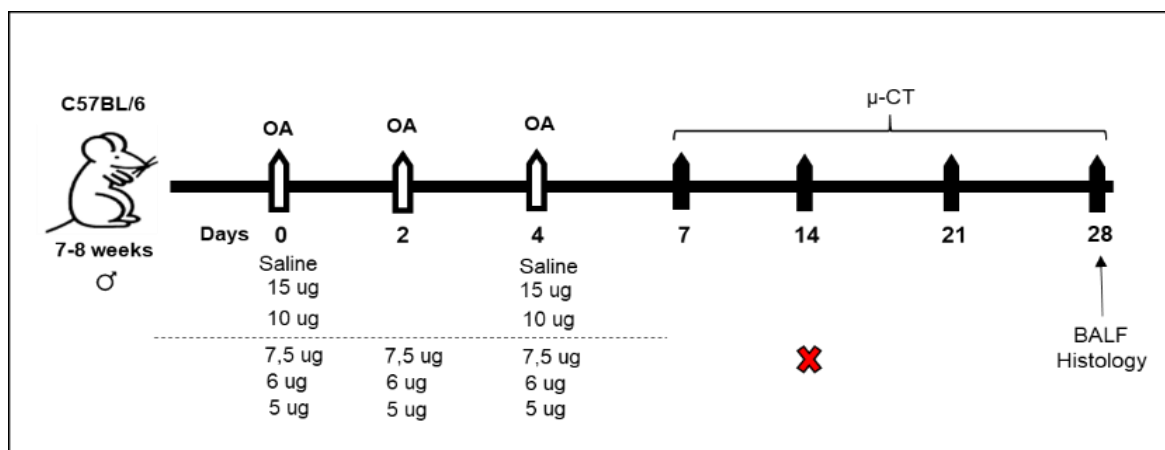


Figure 5: Schematic Representation of the experimental setting. Thirty C57BL/6 male mice were randomized in 6 groups to receive saline, double oropharyngeal administration (day 0 and 4) of 10 or 15 μ g of BLM, and triple OA (day 0, 2, 4) of 5, 6 or 7.5 μ g of BLM. Micro-CT (μ -CT) was performed at days 7, 14, 21 and 28. Animals were euthanized at day 28 to collect BALF and lungs for histology

procedure is shown in Figure 5.

Pharmacological validation: Nintedaninb administration

The model based on triple BLM administration (6 μ g) was selected for further characterization and to study the response to antifibrotic treatment with Nintedanib.

Thirty-five animals received triple dose of BLM and 5 animals received 50 μ L OA of saline as a control. At day 7, BLM-treated mice were randomly divided in three experimental groups

- 1) Twenty-five BLM-treated animals: at selected time points, (7, 14, 21, 28, 35 days) 5 mice were sacrificed at each time point
- 2) Five BLM-treated animals received NINT (60 mg/kg/die p.o.) daily from day 14 to 28
- 3) Five BLM-treated animals received NINT (60 mg/kg/die p.o.) daily from 7 to 28 days

All the animals underwent micro-CT scanning once a week and at the time of sacrifice bronchoalveolar lavage and lungs harvesting was performed (Figure 6).

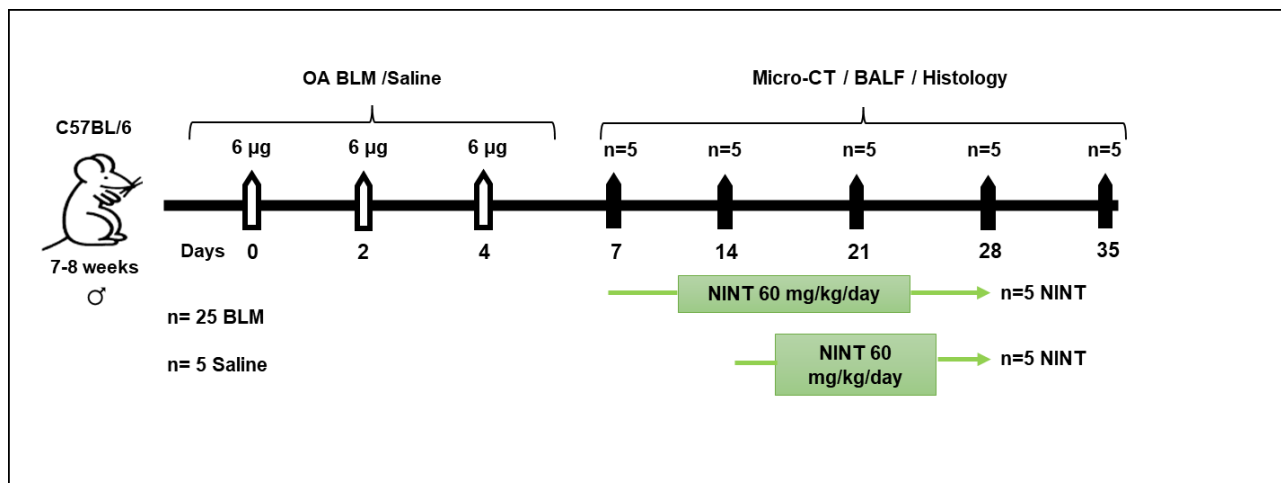


Figure 6: Schematic Representation of the experimental setting for characterization and pharmacological validation. Twenty-five C57BL/6 male mice were received triple OA (day 0, 2, 4) 6ug of BLM. 5 mice received triple OA of 50 ul of saline. At day 7, they were randomized in 3 groups to receive 60 mg/kg/day NINT and Vehicle via gavage from wither day 7 or day 14. Micro-CT (μ -CT) was performed at days 0, 7, 14, 21,28 and 35. 5 animals were euthanized at day 7,14,21,28 and 35 to collect BALF and lungs for histology.

Micro-CT imaging

Micro-CT imaging was performed with Quantum GX Micro-CT (PerkinElmer, Inc. Waltham, MA).

The mice were anesthetized with 2% isoflurane in oxygen and then were positioned supine in micro-CT under the 2% isoflurane during the acquisition.

Images were acquired with an intrinsic retrospective two phases respiratory gating technique with the following parameters: 90 KV, 88 μ A over a total angle of 360° for a total scan time of 4 minutes.

The high-speed respiratory gating technique allows to control the animal breathing thanks to detection of diaphragm movement and as an output for each scan reconstructs two 3D datasets, corresponding to the different phases of breathing cycles, (end-inspiration and end-expiration).

Breathing rate is constantly registered and its stability is controlled during the micro-CT acquisition.

The range of 100-150 breaths per minute (brpm) was considered optimal for mice lung CT acquisition

Analysis of CT scans

The reconstructed datasets were analyzed using Analyze software (*Analyze 12.0; Copyright 1986-2017, Biomedical Imaging Resource, Mayo Clinic, Rochester, MN*).

Exploiting the air as natural contrast inside the lung, a semi-automatic segmentation was used to extract the airway tree and the total lung volumes from each scan. In particular, we used the 'object extractor' tool, which allows to specify a seed point and a threshold range to correctly detect the object in the volume (**Figure 7** and **Figure 8**).

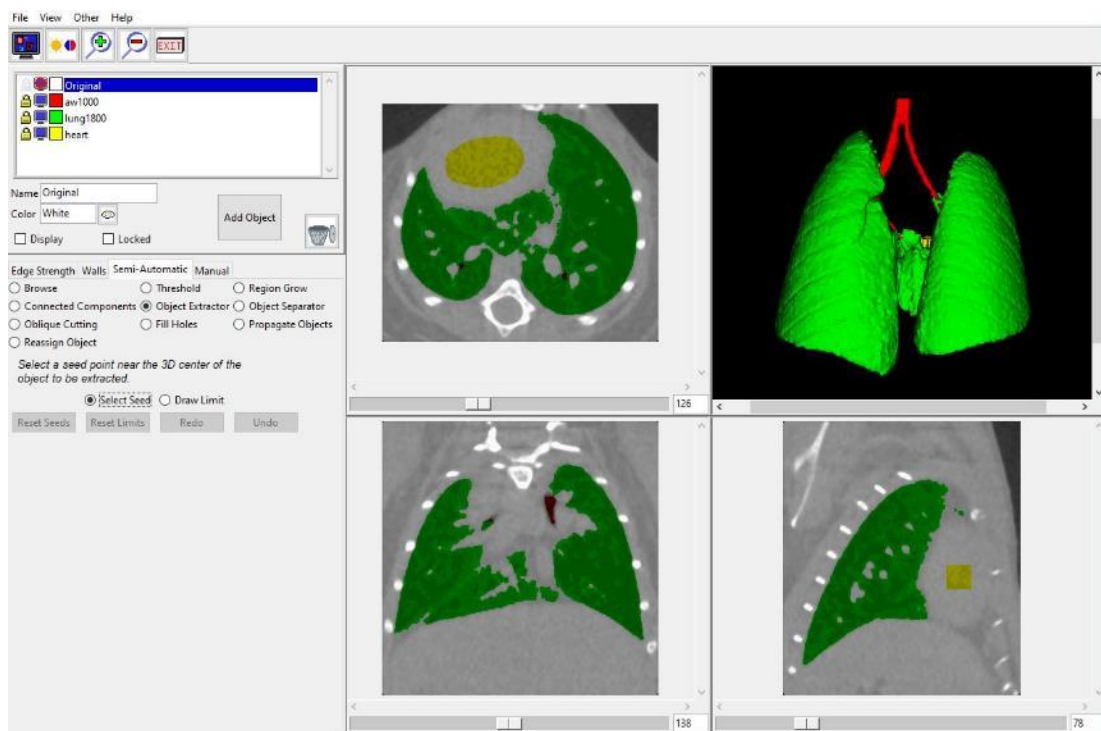


Figure 7: object extractor tool enables to define whole lung volumes in a healthy or uniformly aerated parenchyma.

A manual segmentation of the lung, instead, was necessary to define lung regions that are not detectable due to the lack of aeration, the absence of clear boundaries and the presence of jagged or damaged parenchyma like in fibrotic areas in sick animals (**Figure 9**) (Mecozzi, 2020).

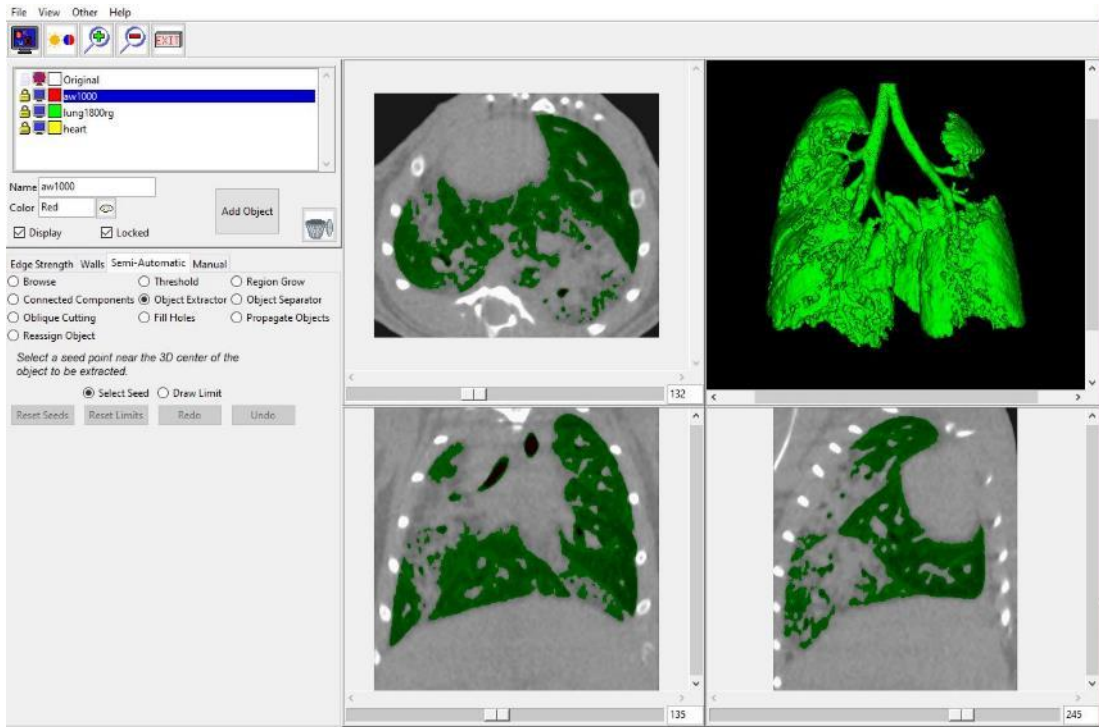


Figure 8: semi-automatic segmentation of a BLM lung. Some dense areas (orange arrows) are not detectable and manual segmentation is required to correctly extract the whole parenchyma.

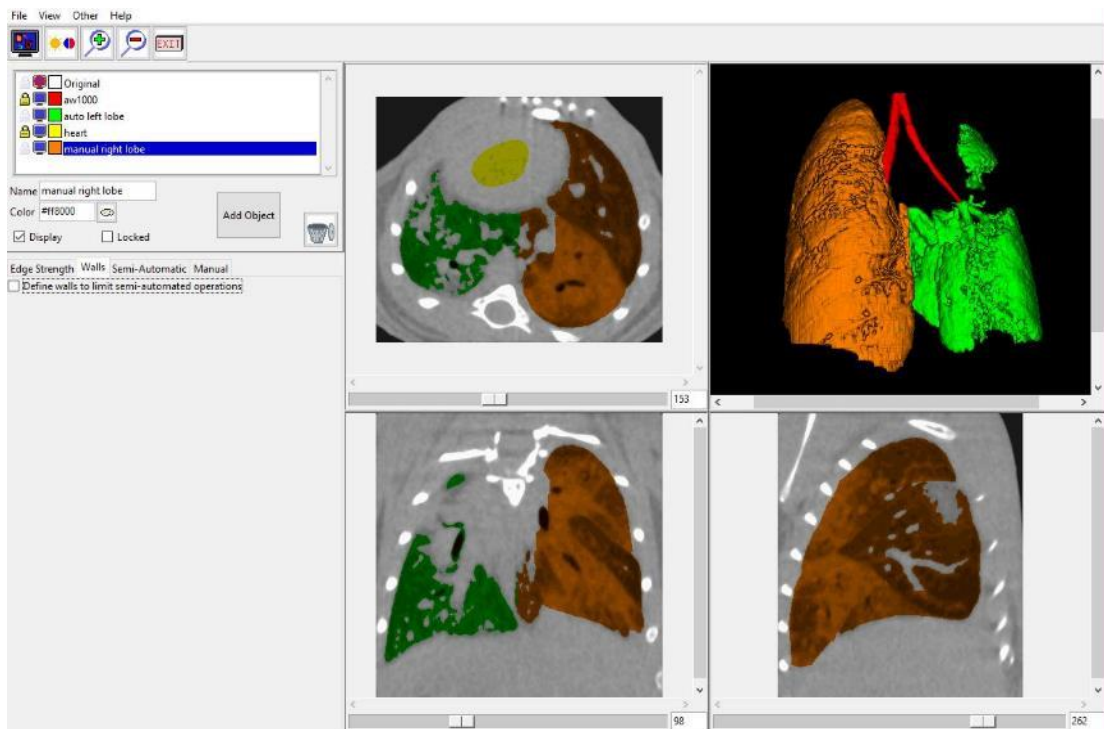


Figure 9: Manual segmentation is required to correctly recreate the whole parenchyma.

After segmentation, micro-CT images were rescaled into Hounsfield units (HU), setting -1000 HU as the density of air and 0 HU as the density of water, to obtain HU frequency distributions (as reported in **Figure 10**). Pre-clinical HU density ranges[62] were applied to semi-automatically or manually

segmented lungs for the quantitative assessment of aeration compartments. Starting from clinical ranges [98], we defined pre-clinical thresholds, specific for mouse lungs segmentation, based on HU frequency distributions of healthy and fibrotic lungs of mice. Thus, hyper-inflated [-1040 HU; -860 HU], normo-aerated tissue [-860 HU; -435 HU], hypo-aerated tissue [-435 HU; -121 HU] and non-aerated tissue [-121 HU; +121 HU] were defined and normalized on total lung volumes. The normo-aerated tissue is the main component of healthy lung (80% in the end-expiration phase) whilst the hypo- and non-aerated tissues are the prevalent components of damaged/fibrotic and low aerated lungs, as shown in **Figure 10**.

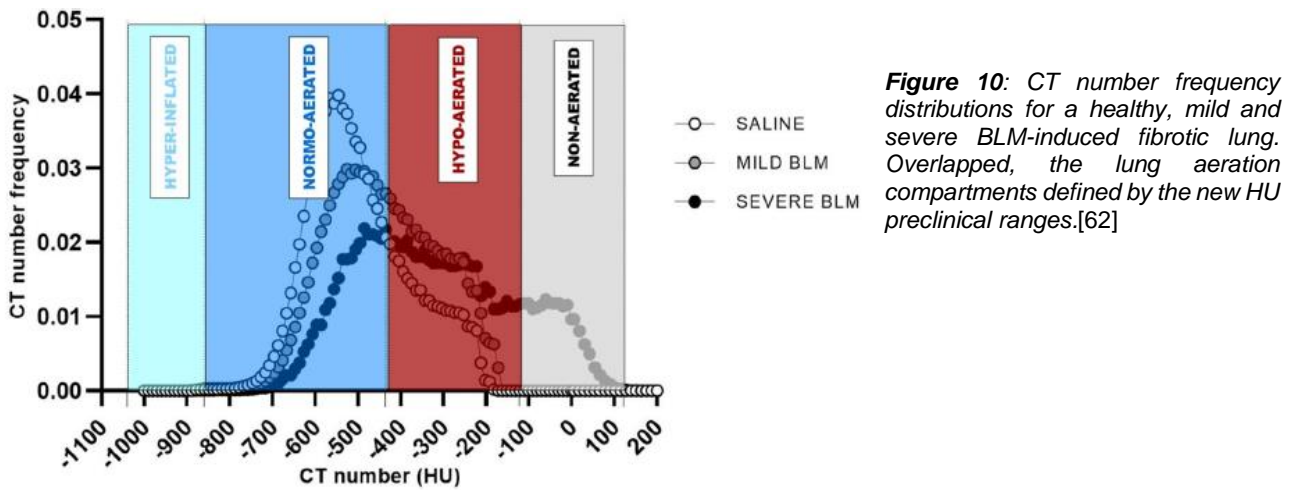


Figure 10: CT number frequency distributions for a healthy, mild and severe BLM-induced fibrotic lung. Overlapped, the lung aeration compartments defined by the new HU preclinical ranges.[62]

From the analysis of both end-inspiration and end-expiration phases, we could extrapolate other interesting lung functional parameters. A list of micro-CT parameters evaluated in this work is reported in **Table 1**.

Parameter	Equation
Functional Residual Capacity (FRC)	(1) $FRC(mm^3) = V_{P02}(mm^3) \frac{MLA_{P02}(HU)}{Air(HU)}$
Air-to-tissue ratio (Ratio)	(2) Ratio = $\frac{Air_{P01}(mm^3)}{Tissue_{P01}(mm^3)}$
	$Air_{P01}(mm^3) = V_{P01}(mm^3) \frac{MLA_{P01}(HU)}{Air(HU)}$ $Tissue_{P01}(mm^3) = V_{P01}(mm^3) - Air_{P01}(mm^3)$

Table 1: Densitometric-based equations of lung function parameters [95]

In particular, the functional residual capacity (FRC) represents the volume of air inside the lung at the end of the expiratory phase, the tidal volume (V_t) is the volume of air ventilated during a single breath (difference between the volume of air at the end-inspiration and that at the end-expiration phase). The air-to-tissue ratio describes, instead, the trend in the relative content of air and tissue into the lung: with respect to a healthy subject, in a fibrotic lung the content of air decreases, along with an augment in tissue and collagen deposition in fibrotic regions, so that its ratio tends to diminish during disease progression.

Bronchoalveolar lavage and cell count

At the endpoint, mice were euthanized by anesthetic overdose followed by abdominal aorta bleeding. Bronchoalveolar lavage fluid (BALF) was collected by gently washing the lungs with 0.6 mL of sterile solution [Hank's balanced salt solution x10; ethylenediaminetetraacetic acid 100mM; 4-(2-hydroxyethyl)-1-piperazineethansulphonic acid 1mM; distilled water] for three times in the bronchial tree. The cell pellet was resuspended in 0.2 mL of PBS and white blood cells (WBC) were counted with an automated cell counter (Dasit XT 1800J, *Sysmex*) as the subpopulations (macrophages, lymphocytes and neutrophils). The supernatants were freeze at -80 for further investigation.

Matrix metalloproteinases and TIMPs measurement

MMPs and TIMPs were measured using costume Bio-plex assay (Bio-Techne)[99] to measure MMP-2, MMP-8, MMP-12, TIMP-1 and TIMP-4 in the supernatants. The assessment was performed according to the manufacturer's instructions using all the reagents and wash buffers provided by the kit. The assay was analysed by Bio-Plex 200 and the concentration for each mediator was interpolated from standard curves using version 5.0 of Bio-Plex Manager software provided by Bio-rad.

Histological staining on lung tissue sections

Lungs were gently inflated with 0.6 mL of 10% neutral buffered formalin using a cannula through the trachea and then excised. After 24h lungs were dehydrated in graded ethanol series, clarified in xylene and paraffin embedded. For each lung, sections of 5 μm thickness were cut at 200 μm

intervals, using a rotary microtome (Slee Cut 6062, *Slee Medical, Mainz, Germany*). Hematoxylin and eosin (H&E) and Masson's trichrome staining were performed for each slide.

The slides were acquired by a NanoZoomer S-60 Digital slide scanner (NanoZoomer S60, *Hamamatsu, Japan*) and morphological changes or alterations in lung sections were graded semi-quantitatively according to the scale defined by Ashcroft and modified by Hübner et al[100]. by two independent researchers blinded to the experimental design.

Results

Setting up the optimized murine lung fibrosis model

First, we have tried to identify the ideal BLM dose regimen to set up a lung fibrosis model with an appropriate balance between sustained lung fibrosis up to 28 days and animal welfare in C57Bl/6 male mice, using the micro-CT power to perform longitudinal in vivo assessment and reducing the animal number.

Clinical observation

BLM instillation caused a dose-dependent body weight drop. Figure 11 shows the body weight variation during the experiment. The reduction of body weight remained within 10% till day 14 for all groups, except the groups treated three times with 7,5 ug of BLM, in which the animals lost 20% of initial weight within the first 2-weeks.

Thus, in agreement with the designated veterinarian and the internal Animal Welfare Body, this group of mice was sacrificed and excluded from the study (Fig 11A). All the mice receiving either BLM double or triple OA showed a recovery in body weight at later time-points, regaining the initial body weight at day 28, except for the group receiving a double dose of 15 µg whose body weight remained

unaltered from day 14 to day 28. Among these groups, no mortality was observed. Control mice treated with saline gained weight, as expected, during the time of observation (Fig 11B).[97]

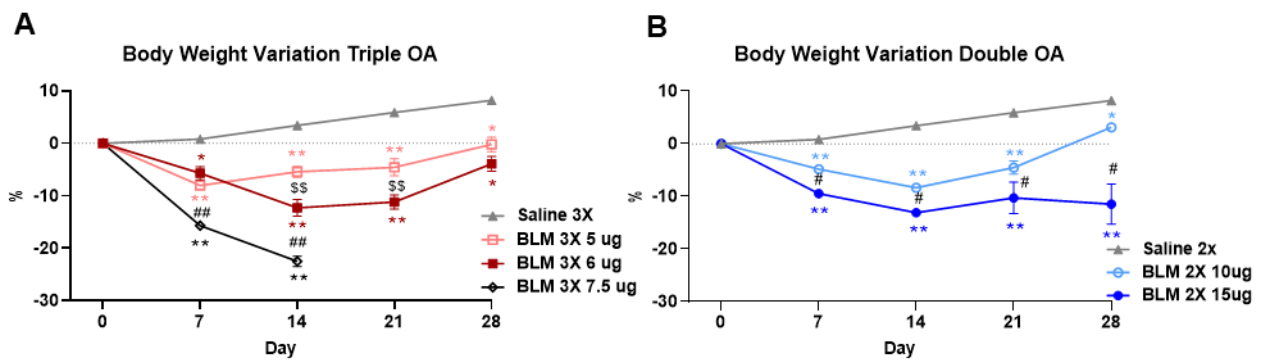


Figure 11: Body weight variation. BW was reported as the percentage of variation compared to the baseline (day 0) for saline, double OA (B) and triple OA (C) groups. Data were shown as mean \pm SEM. Statistical analysis was performed via two-way ANOVA followed by Tukey's test * $p < 0.05$, ** $p < 0.01$ vs. saline; # $p < 0.05$, ## $p < 0.01$ comparing 10 μ g vs. 15 μ g BLM and 5 μ g vs. 6 μ g BLM; \$\$ $p < 0.01$ comparing 7.5 μ g vs. 6 μ g BLM). N = 5 per group

Micro-CT analysis

All mice were scanned by micro-CT longitudinally at day 7, 14, 21, 28. Representative coronal micro-CT lung slices and the corresponding 3D renderings of BLM and saline-treated animals at different time points are reported in Fig 12A. As expected, the saline group had 77–80% normo-aerated tissue with 20–23% hypo-aerated tissue throughout the study (Fig12A'). Those receiving three doses of 7,5 μ g of BLM has shown scared tissues at day 7 which reached an exaggerated level at day 14, the experiment for this group was ended at day 14 based on animal welfare and to avoid any further pain for the animals. The representative coronal images together with 3D rendering demonstrated the localization of non -aerated tissue in upper area of both right and left lobes from day 7 (Fig12B-B').

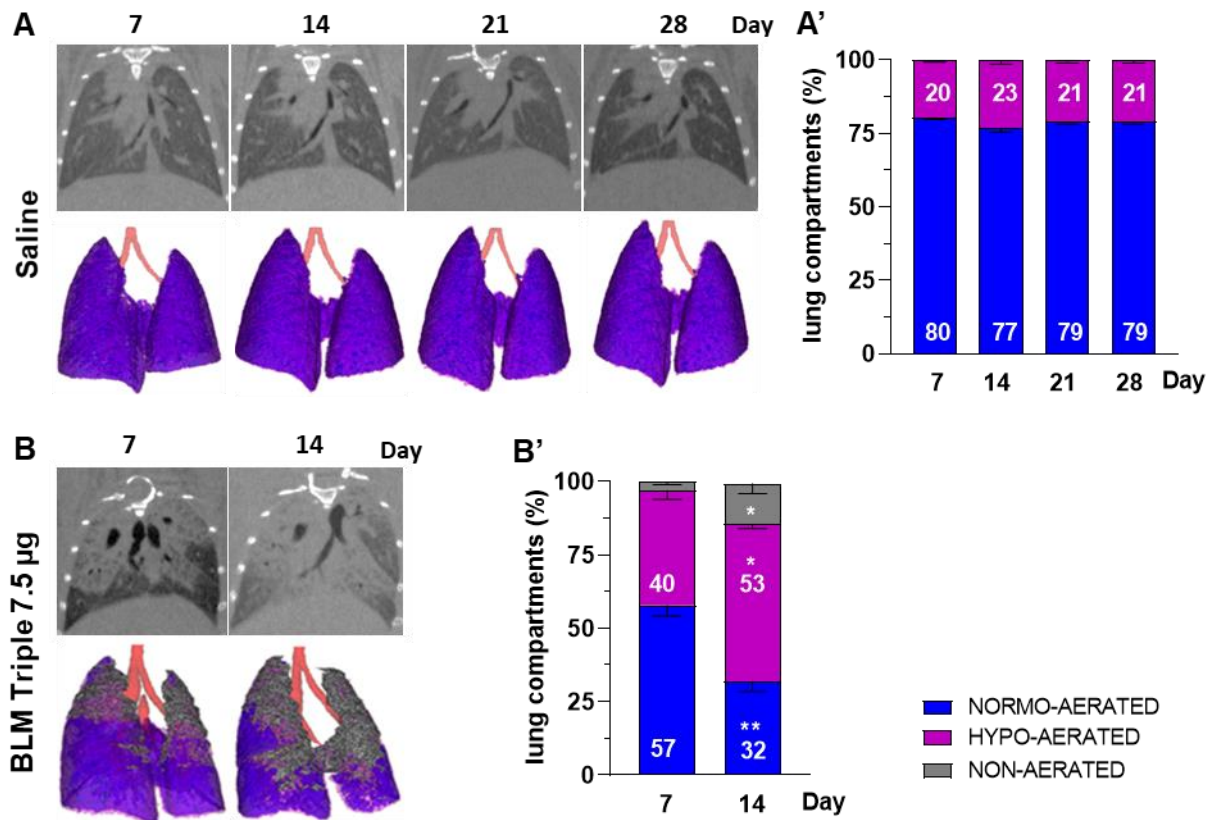


Figure 12: Longitudinal micro-CT results in saline and triple OA of 7.5 µg BLM group. (A) Representative coronal micro-CT lung slices and 3D renderings at the end of expiration phase of saline at 7, 14, 21 and 28 days. (A') Lung aeration degrees expressed as percentage of normo-, hypo- and non-aerated tissues detected at 7, 14, 21, 28 days for the saline group. (B) Representative coronal micro-CT lung slices and 3D renderings at the end of expiration phase of triple OA of 7.5 µg BLM group at 7 and 14 days. (B') Lung aeration degrees at 7 and 14 days for the triple OA of 7.5 µg BLM group. Data are shown as mean ± SEM. The statistical differences were calculated by two-way ANOVA followed by Tukey's test (** $p < 0.01$ vs. saline). $N = 5$ per group

Animals treated with a double OA of 10 µg BLM showed a significant increase ($p < 0.05$) in hypo-aerated tissue compared to saline at 14 and 21 days, which was no longer observed at day 28. Non-aerated lung tissue, corresponding to more severely damaged areas, was between 4–6% of the whole parenchyma since day 14, and remained stable up to the end of the study, not being significantly higher than in the saline group (Fig 13B). The double administration of 15 µg BLM caused a marked increase ($p < 0.01$) of hypo-aerated tissue from day 14 to day 28, followed by a significant augment of non-aerated areas ($p < 0.01$) at day 21 and 28 (Fig 13C). As regards mice treated with the triple dose regimen, those receiving 5 µg BLM showed an increased hypo-aerated tissue between days 14–28 ($p < 0.01$), whilst non-aerated areas remained at about 4% of the lung parenchyma in the same time frame, without reaching statistically significant difference with respect

to the saline group (Fig13D). On the other hand, the group receiving 6 μg BLM had a significantly higher hypo-aerated tissue already at day 7 and lasted at all the observed time-points ($p < 0.01$), besides showing a marked increase in non-aerated areas at day 21 ($p < 0.05$) (Fig 13E).

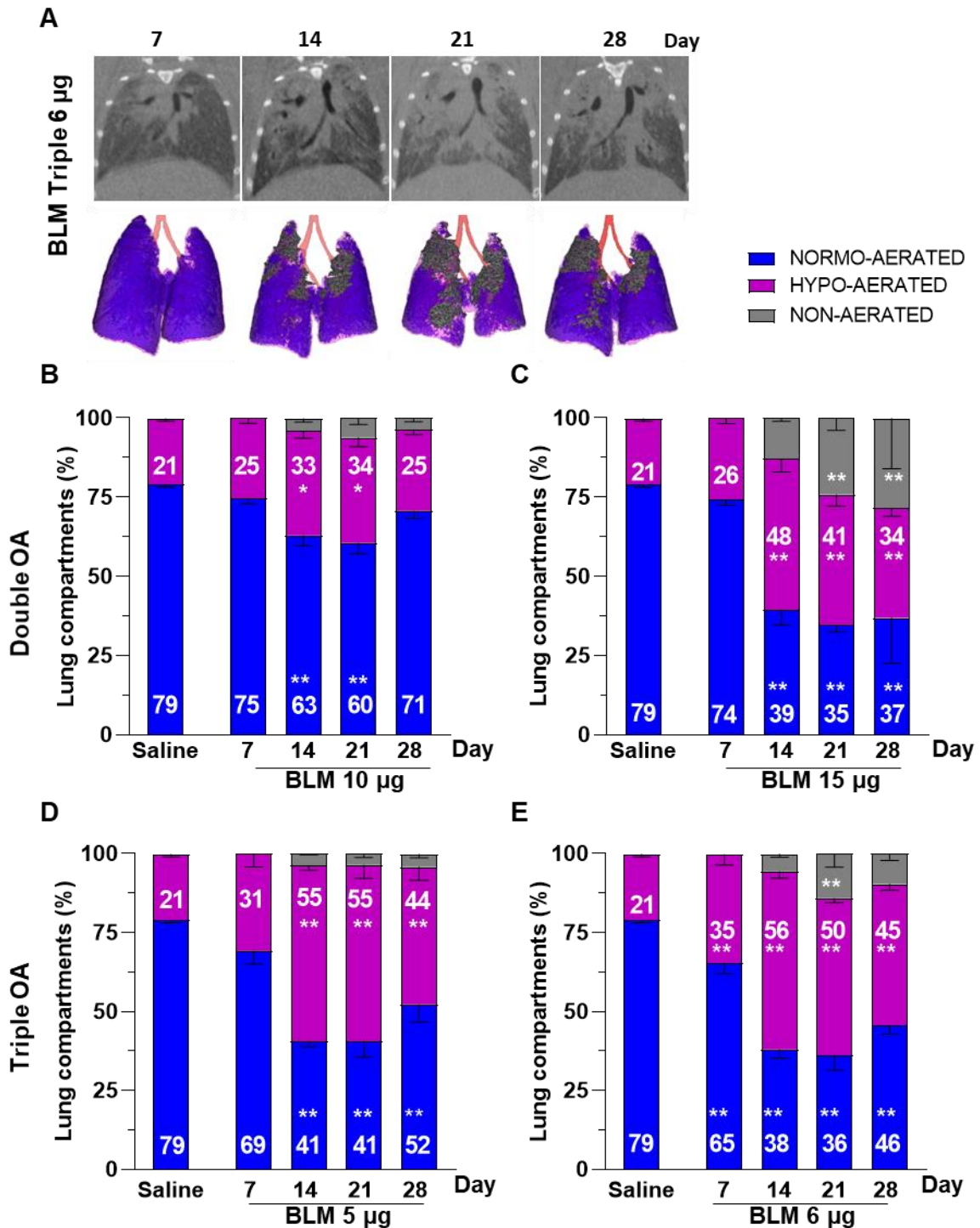


Figure 13: Longitudinal micro-CT assessment. (A) Representative coronal micro-CT lung slices and 3D renderings at the end of expiration phase of saline- and BLM-treated mice at 7, 14, 21 and 28 days. (B-E) Lung aeration degrees expressed as percentage of normo-, hypo-, and non-aerated tissues detected at 7, 14, 21, 28 days for the saline group and BLM groups at different dose regimens. Data are shown as mean \pm SEM. The statistical analysis was performed for each group compared to saline via two-way ANOVA followed by Dunnett's test (* $p < 0.05$; ** $p < 0.01$ vs. saline). $N = 5$ per group.

Animals treated with a double dose of either 10 or 15 µg BLM had a significantly higher ($p < 0.01$) lung volume with respect to saline at days 7 and 14, whilst no differences between groups were seen at days 21 and 28 (Fig 14A). On the other hand, mice receiving the triple OA of BLM at both doses had a prominent increase of lung volume at day 7 ($p < 0.01$), whereas from day 14 no significant differences were revealed compared to saline (Fig 14B). As regards the air/tissue ratio, at day 7 no differences between the groups receiving double BLM and saline were revealed. However, a markedly lower ratio ($p < 0.01$) was observed in mice receiving either 10 or 15 µg BLM at days 14 and 21. Between days 21 and 28, the air/tissue ratio slightly increased in the 10 µg group but was not significantly different than in saline at day 28. In the 15 µg BLM group the ratio stabilized from 21 to 28 days, being still considerably lower with respect to saline ($p < 0.01$) at the final time-point (Fig 14C). In the groups subjected to triple OA no differences were detected at day 7 in the air/tissue (Fig 14D). The ratio significantly decreased in fibrotic mice dosed with either 5 or 6 µg from 14 to 21 days ($p < 0.01$). Although a slight increase at 28 days was observed, the parameter remained significantly lower compared to saline ($p < 0.05$ for 5 µg and $p < 0.01$ for 6 µg) (Fig 14D).

Figures 14E and 14F show FRC normalized on total lung volumes. FRC/V_{exp} was not affected by either double or triple BLM administration at 7 days. However, from day 14 to 21 a significant decline was observed in all BLM-treated groups compared to saline mice ($p < 0.01$). At day 28, FRC/V_{exp} remained significantly lower compared to saline ($p < 0.01$) in all BLM-treated groups, except for the group receiving the double dose of 10 µg BLM which was reinstated (Fig 14E).

As expected, the total lung volume and functional respiratory biomarkers were constant for the saline group throughout the study.[97]

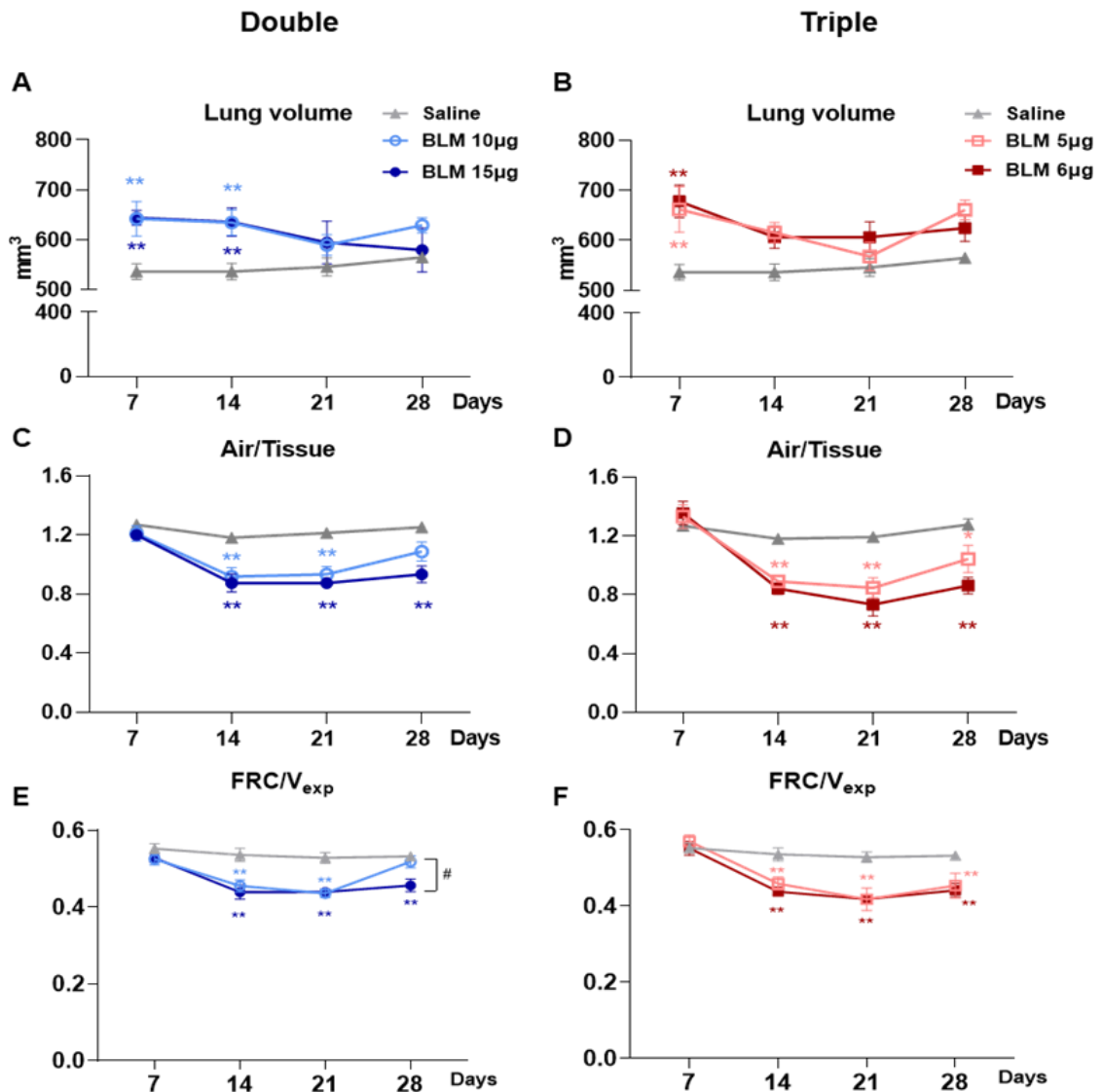


Figure 14: Longitudinal lung function readouts. Longitudinal analyses of the lung volume detected by micro-CT in mice treated with double (A) or triple (B) doses of BLM, compared with the saline group. Longitudinal quantification of air/tissue ratio in double (C) or triple (D) doses of BLM. Longitudinal quantification of FRC/V_{exp} in double (E) or triple (F) doses of BLM. Data are shown as mean ± SEM. The statistical differences were calculated by two-way ANOVA followed by Tukey's test (*p < 0.05; **p < 0.01 vs. saline group. ## p < 0.01 comparing 10 µg vs. 15 µg BLM). N = 5 per group.

Inflammatory cells infiltration count

At day 28, after the animals' euthanasia, the BALF was harvested and leukocytes were counted. As expected, the total WBC was significantly increased in all the groups receiving BLM, compared with saline (p < 0.01) (Fig 15A and 15D). A significant difference was revealed between the two groups treated with the triple BLM dose (Fig 15D), as the WBC count was much higher following the administration of 6 µg (p < 0.01). As concerns leukocyte subpopulations, macrophages were

markedly higher in the group receiving the double dose of 15 μg BLM compared to saline ($p < 0.05$), whereas the double dose of 10 μg evoked a moderate, non-significant increase (Fig 15B). On the other hand, triple OA treatment with BLM induced a prominent increase in macrophages ($p < 0.05$) at both doses compared to the saline group (Fig 15E). Following the double administration of BLM, lymphocytes were significantly increased compared to the saline group ($p < 0.05$) (Fig 15C). On the other hand, the triple dose of 5 μg BLM slightly increased lymphocytes, although not significantly, versus saline, whereas in mice receiving the triple dose of 6 μg markedly higher levels of lymphocytes were observed ($p < 0.01$) as compared with either the saline or the 5 μg BLM groups (Fig 15F).[97]

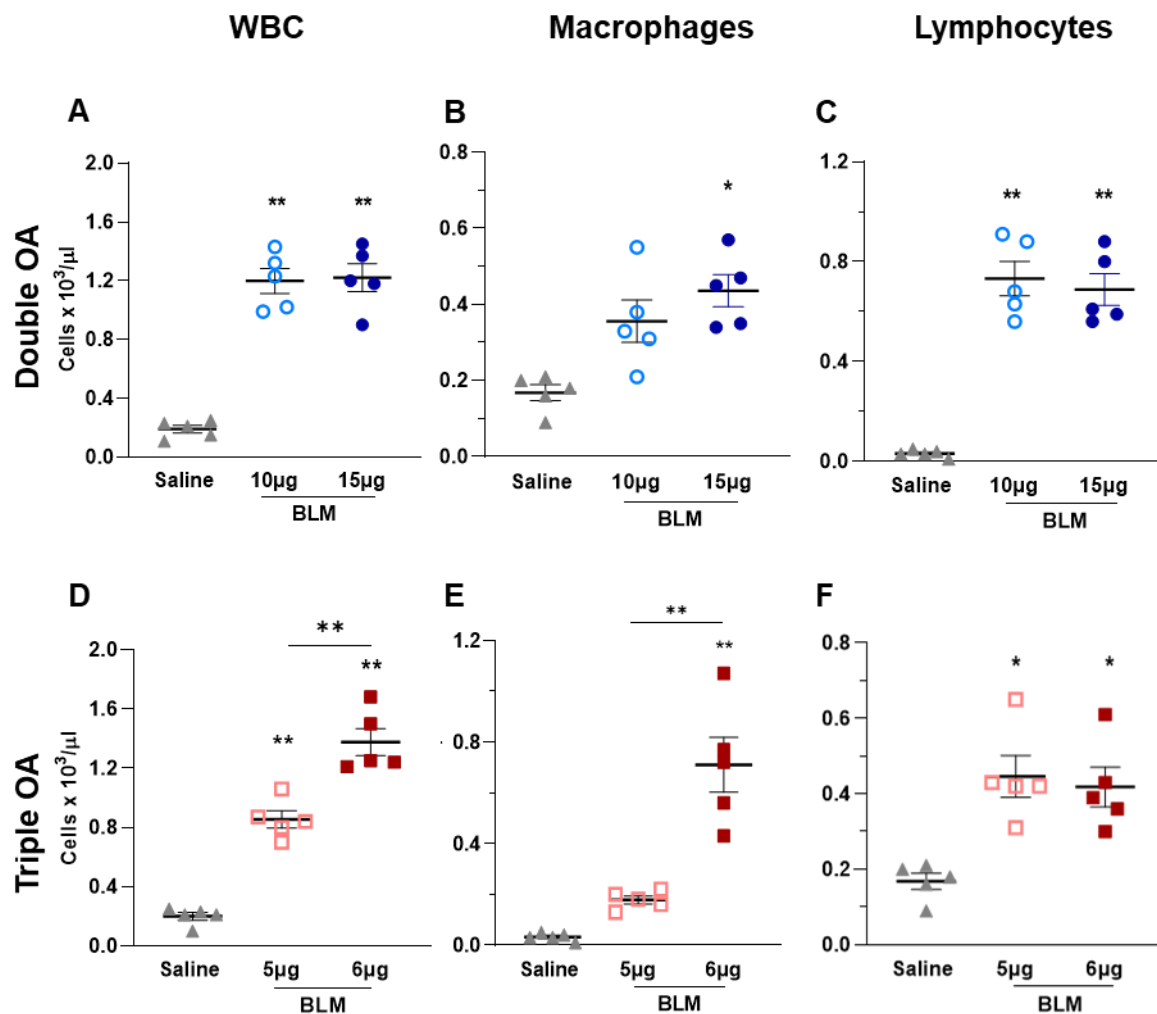
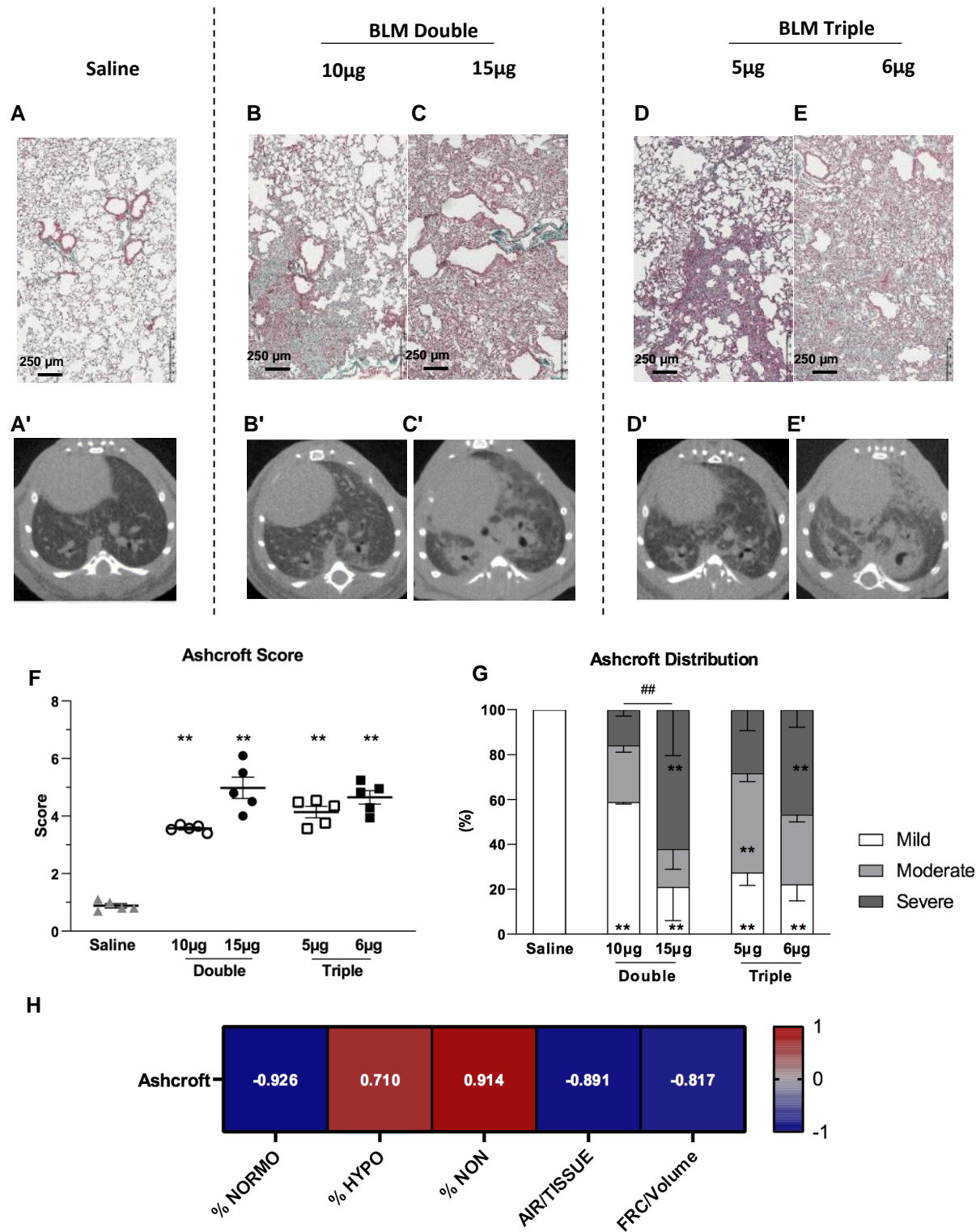


Figure 15: Inflammatory cells infiltration in BALF. Levels of total white blood cells (A, B), macrophages (C, D) and lymphocytes (E, F) in BALF of animals receiving saline, double and triple doses of BLM. Data are shown as mean \pm SEM. Statistical significance was calculated between the animal groups by one-way ANOVA followed by Tukey's test (* $p < 0.05$; ** $p < 0.01$). $N = 5$ per group.

Histological evaluations

Histological pictures of the lungs stained with MT of saline and BLM-treated groups are presented in figure 16 A-E. As expected, both double (10, 15 µg) and triple (5, 6 µg) BLM treatment caused patchy fibrotic alterations of lung parenchyma characterized by fibroproliferative foci with various degrees of confluence at 28 days (Fig16 B-E). On contrary, any parenchymal alteration was reported in the saline group Fig 16 A. The corresponding transversal micro-CT scans of the mice reported in the above histology are shown in Figure 16 A'-E'. The mean Ashcroft Score was significantly increased ($p < 0.01$) in all groups receiving BLM compared to the saline group (Fig 16F). No statistically significant differences were revealed between BLM-treated groups. To better reflect the morphological alteration of the lung parenchyma, the Ashcroft score was reported as the frequency distribution of mild (0–3), moderate (4), and severe (≥ 5) fibrotic lesions (Fig 16G) [101] The double (10 µg) BLM treatment induced moderate to severe fibrosis with respect to the saline group, but within a limited area of parenchyma (Fig 16B). On the other hand, in all the other groups treated with BLM a more distributed injury in lung parenchyma was evident (Fig 16C-E), with the presence of both moderate and severe fibrosis. In particular, the highest % severe fibrosis was observed in mice receiving the double dose of 15 µg ($62 \pm 20\%$) and the triple dose of 6 µg ($47 \pm 8\%$). Between the two groups receiving a double OA of BLM a significant difference in terms of Ashcroft frequency distribution was revealed ($p < 0.01$).

Spearman correlations between micro-CT readouts and Ashcroft score were performed (Fig 16H). Positive and negative significant correlations with high Spearman coefficients were obtained ($p < 0.05$) for all CT readouts, except for lung volume (Spearman coefficient = 0.007, $p > 0.05$, data not shown).[97]



Time course characterization of triple OA of 6µg of BLM-lung fibrosis model and its response to three weeks of NINT treatment.

The triple administration of 6 µg of BLM was identified as an optimal dose regimen to combine sustained fibrosis with animal welfare. We decided to characterize this protocol at days 7, 14, 21, 28 and extended further to day 35 to verify the presence of fibrotic features at this timepoint.

Twenty-five animals received triple dose of BLM and 5 animals were sacrificed at each timepoint.

Clinical observation

The animal's body weight and clinical manifestations were checked, and BW reported in figure 17. As we have shown in the dose-finding experiment, the body weight lost was limited to 10± 0.5% of the starting BW, with a peak 16 days upon the first BLM administration ($p < 0.01$). A recovery in the BW was observed in the BLM group since day 24 and the starting BW was recovered at day 30.

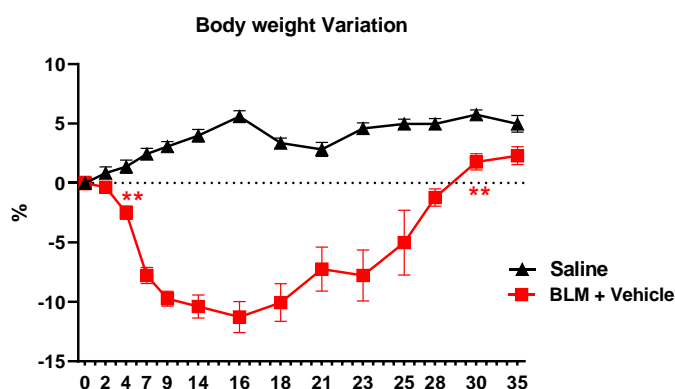


Figure 17: Body weight variation. BW was reported as the percentage of variation compared to the baseline (day 0) for triple BLM treated with vehicle, and Saline. Data are shown as mean \pm SEM. Statistical analysis was performed via two-way ANOVA followed by Tukey's test * $p < 0.05$, ** $p < 0.01$ vs. Saline; The statistical differences was found from day 4 to 30.

Micro-CT analysis

All the mice underwent micro-CT scans at days 7, 14, 21, 28, and 35. The lung aeration degrees were calculated for each animal and shown longitudinally in Figure 18.

As we demonstrated, the normally-, Hypo- and non-aerated tissue in saline remains stable throughout the experiment (Fig 12A). The triple administration of 6 µg of BLM confirmed a significant decrease of normally aerated tissue from day 14 to 28 compared to saline ($p < 0.01$), Although at day

35 there is a tendency to return to the normal values observed in saline mice, the non-aerated tissues is still present however, the hypo-aerated tissue demonstrated the complementary trends, the BLM group confirmed the significantly higher percentages of hypo-aerated tissue from day 14 to 28 compared to saline ($p < 0.01$).

The progressive increase of non-aerated tissue reached a significant level in the vehicle-treated group at day 21 compared to saline ($p < 0.01$).

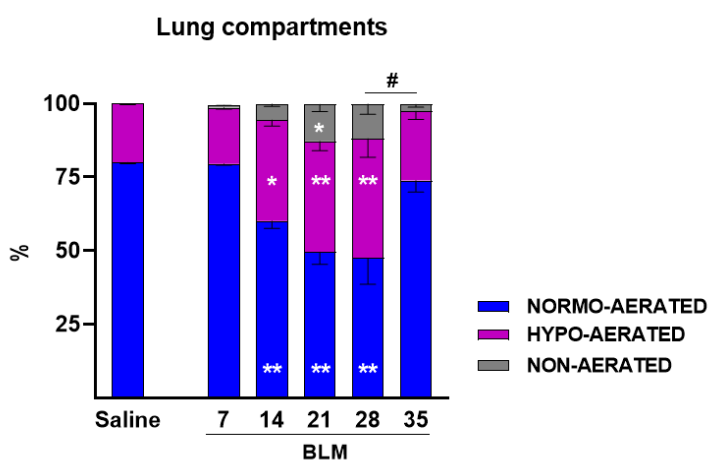


Figure 18: Longitudinal micro-CT assessment. Longitudinal lung aeration degrees expressed as percentage of normo-, hypo-, and non-aerated tissues at days 7, 14, 21, 28, 35. Data are shown as mean \pm SEM for saline group and BLM groups treated with vehicle. The statistical analysis was performed for each group compared to BLM-vehicle via Two-way ANOVA followed by Tukey's test (* $p < 0.05$; ** $p < 0.01$ vs. saline) (# $p < 0.05$ BLM day 28 vs day 35). $N = 5$ per group.

BALF: inflammatory cells

Five animals per each group were sacrificed at days 7, 14, 21, 28, and 35 and BAL fluid was collected for inflammatory cell counting. As expected, the total WBC count showed an increasing trend from day 7 with a maximum peak at day 21 which remained significantly higher compared to saline till day 28 ($p < 0.01$) but not day 35. Leukocyte differential counts revealed significant presence of macrophages at days 7, 14, 28 and 35 ($p < 0.01$) which was found less present in BAL fluid at day 21 ($p > 0.05$). The lymphocyte subpopulation was significantly augmented from day 7 to day 28 ($p < 0.01$) (Fig 19 A-C).

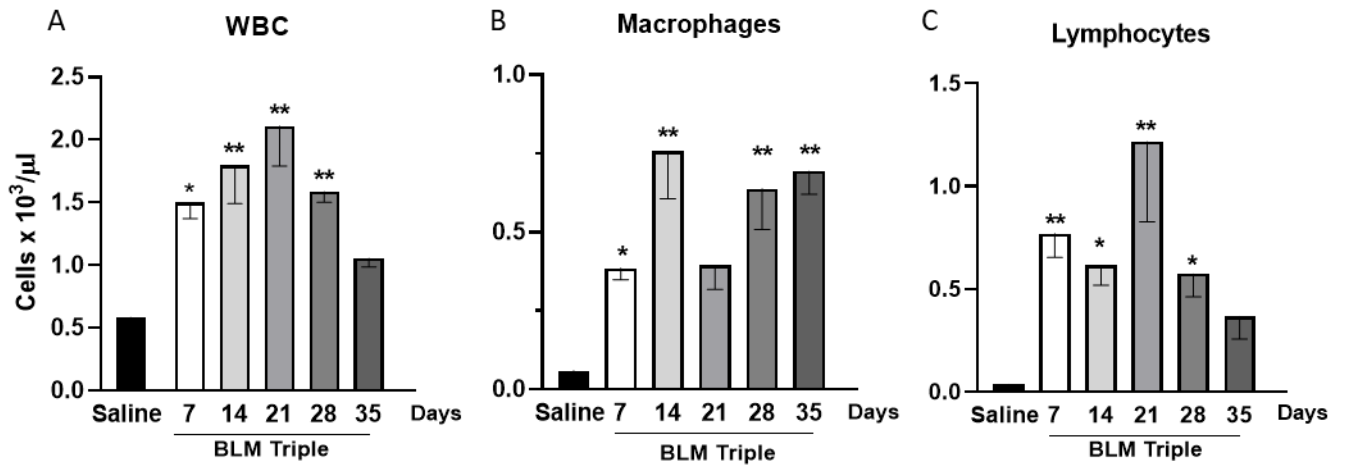


Figure 19: Inflammatory cells infiltration in BALF. Levels of total white blood cells (A), macrophages (B) and lymphocytes (C) in BALF of groups of BLM treated with vehicle at days 7, 14, 21, 28, 35. Data are shown as mean \pm SEM. The statistical analysis was performed for each group compared to saline and different timepoints via one-way ANOVA followed by Tukey's test (* $p < 0.05$; ** $p < 0.01$ vs. saline). $N = 5$ per group.

BALF: matrix metalloproteinases

MMP-2, -8, -12, Timp-1 and Timp-4 were quantified in BALF and normalized on saline at each time point (Fig 20 A-E). The significant increase of MMP-2 compared to saline from day 7 ($p < 0.01$) to 35 reached at the highest level (39 FOI/Saline) at day 21. We highlighted its significant reduction at day 35 compared to day 28 ($p < 0.05$). MMP-8 augmented significantly from day 14 ($p < 0.05$) to day 28 compared to saline and decreased at day 35. MMP-12 was found extremely modulated from day 7 on, which reached 172-Fold higher than saline at day 21 ($p < 0.01$).

TIMP-4 was significantly increased from day 14 with the highest amount at day 21 compared to saline ($p < 0.01$). From day 21, the Timp-4 tends to decrease gradually, but its level remained significantly higher at day 35 compared to saline ($p < 0.05$). Moreover, TIMP1 was found significantly upregulated at days 14 and 21, while it reduced significantly at days 28-35.

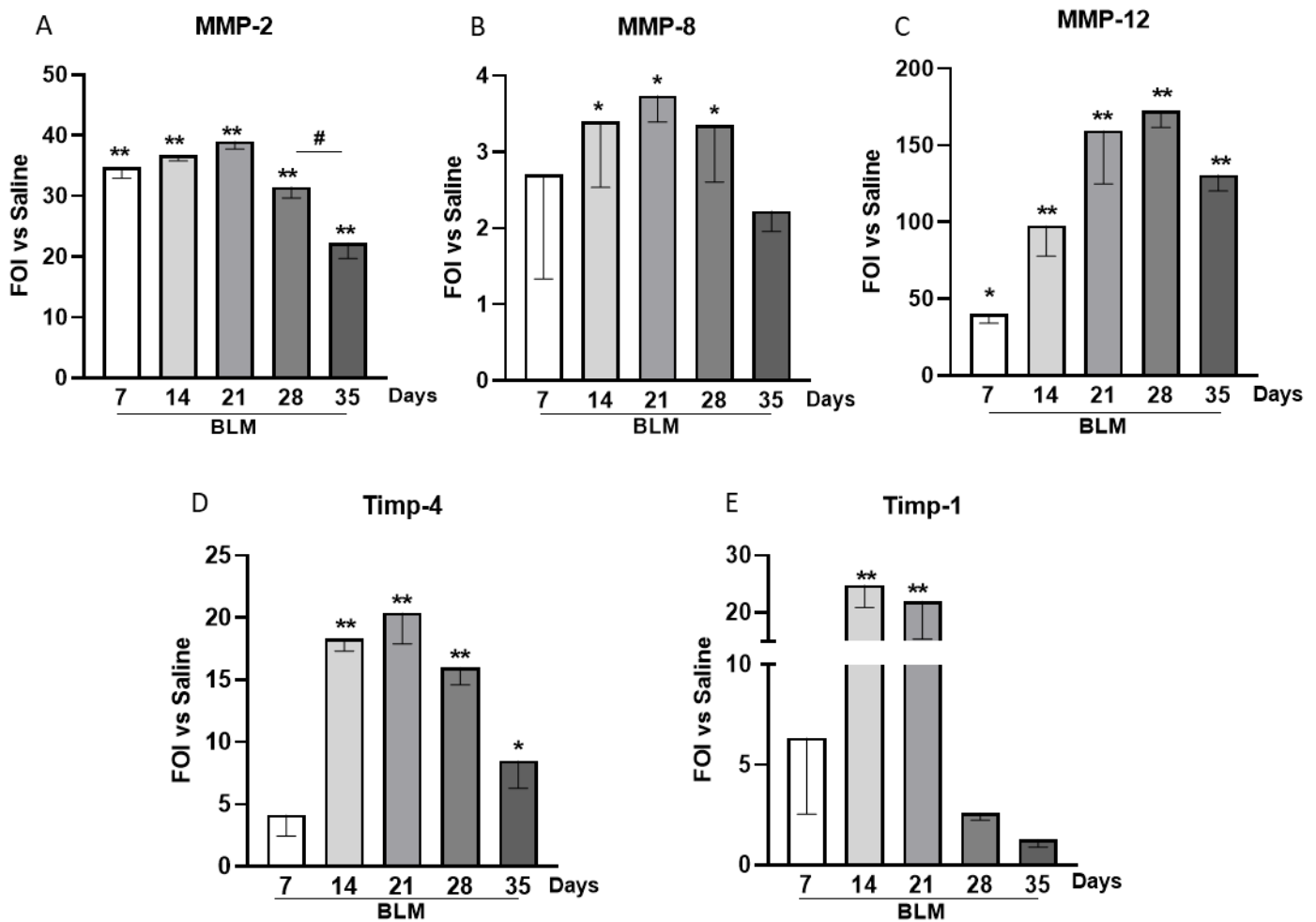


Figure 20: MMPs and TIMPs quantification in BALF. MMP-2, -8, -12 and Timp-4, -1 (A-E in BALF from animal groups of BLM treated with vehicle at different timepoints. Data are shown as FOI vs saline \pm SEM. The statistical analysis was performed for each group compared to saline and different timepoints via one-way ANOVA followed by Tukey's test * $p < 0.05$; ** $p < 0.01$ vs. saline; # $p < 0.05$, ## $p < 0.01$ comparing different timepoints. $N = 5$ per group.

Histological evaluation

The histological pictures of the whole lung stained with the MT and the corresponding higher magnified micro-photographs of the Vehicle-treated group at days 7, 14, 21, 28, 35 are shown in fig 21 A-F'. The histological slides demonstrated the progressive patchy fibrotic alteration in lung parenchyma caused by BLM with the most evident architectural modification and collagen deposition from days 14 to 28. The mean calculation of the Ashcroft score at each time point is shown in fig 21G. Ashcroft's score was found significantly higher after BLM treatment from day 7 on ($p < 0.01$) and remained significantly higher till day 35 ($p < 0.01$). The classification of fibrotic lesions into mild (0–3), moderate (4), and severe (≥ 5), confirmed the significant presence of severely-injured tissue at days 14 ($p < 0.01$), 21 ($p < 0.05$), 28 ($p < 0.01$) compared with saline. Moreover, they were found significantly

different compared to day 7 due to major severely altered fibrotic areas. The Ashcroft distribution quantification confirms the micro-CT data at day 35, we found a limited percentage of severely altered tissue with a high percentage of mild-injured tissue at this time which differs significantly from day 28 ($p < 0.05$).

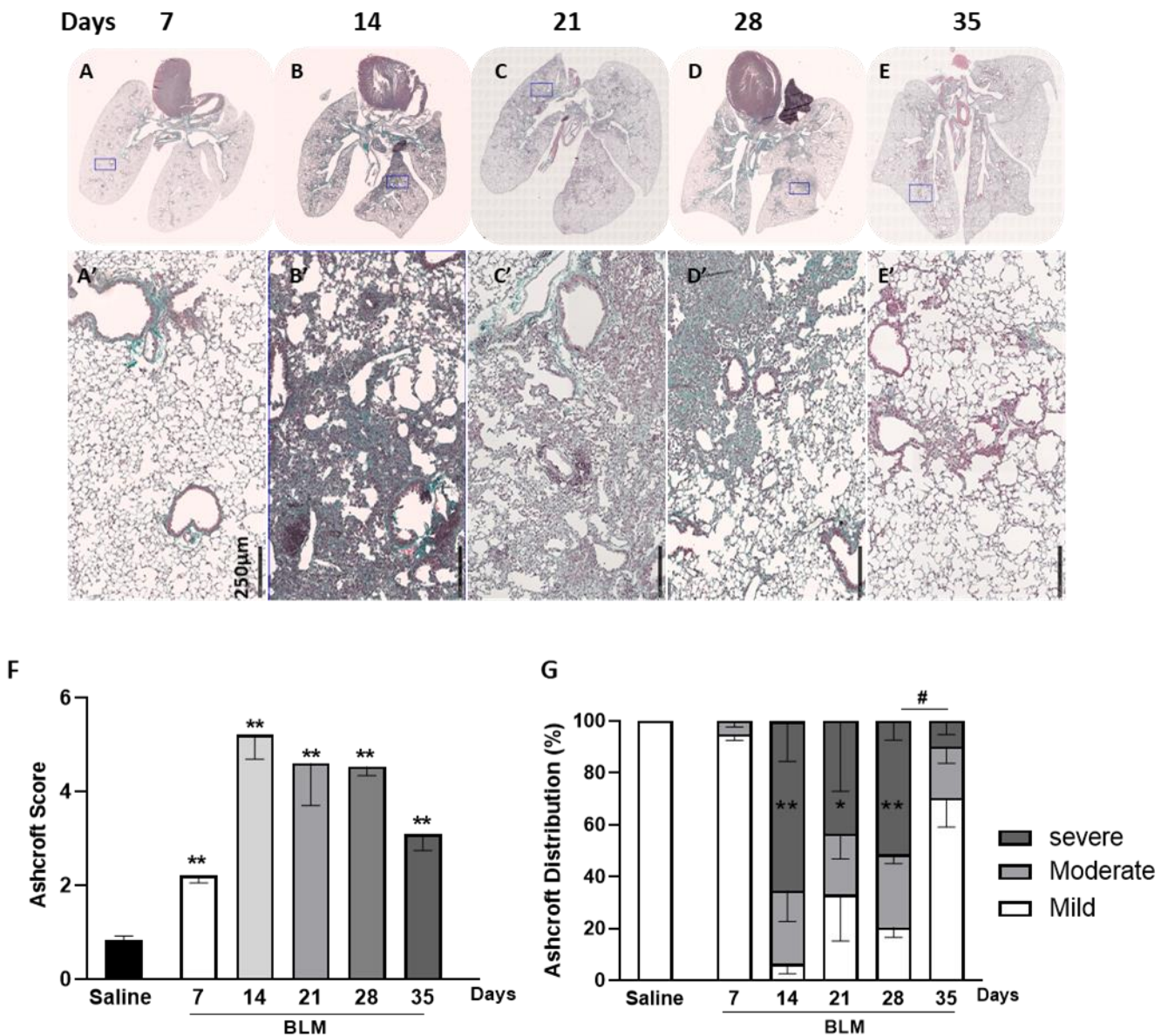


Figure 21: Histological staining. Representative micro-photographs of BLM-tripl group at days 7, 14, 21, 28, 35(A, E) stained with Masson's trichrome. The squares indicate the selected zone with higher magnification (A'-E'). (F) Ashcroft score for the saline, BLM group from days 7-35. (G) Ashcroft frequency distribution in saline and treatment groups. Data are shown as mean \pm SEM. Statistical analysis was performed between the saline and different timepoints by one-way ANOVA followed by Tukey's test (* $p < 0.05$, ** $p < 0.01$ vs. saline; # $p < 0.05$ ## $p < 0.01$ comparing different timepoints. $N = 5$ per group.

Evaluation of antifibrotic response to Nintedanib following different therapeutic schedules

The model based on triple OA of 6 µg of BLM was used to investigate the response to antifibrotic reference compound (NINT) following two schemes of administration

- 1) Nintedanib administration starting after the acute inflammatory phase (days 14-28) (n=5)
- 2) Nintedanib administration starting during the acute inflammatory phase (days 7-28) (n=5)

Clinical observation

The animal's body weight change is shown in Figure 22. All groups have been shown the same body weight decline till day 7.

The mice treated with NINT from 7 to 28 days, showed a significant body weight decrease compared to other groups from day 14 to 21 days, recovering weight in the last week.

By contrary the animals treated with NINT from day 14 to 28 days did not show body weight reduction compared to BLM group, however, no mortality was reported during the experiment.

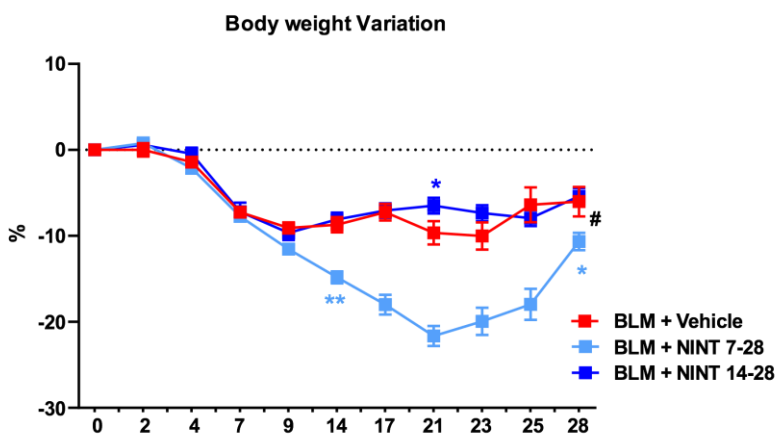


Figure 22: Body weight variation. BW was reported as the percentage of variation compared to the baseline (day 0) for triple BLM treated with vehicle, triple OA with NINT treatment from day 7-28 e from day 14- 28. Data are shown as mean \pm SEM. Statistical analysis was performed via two-way ANOVA followed by Tukey's test * $p < 0.05$, ** $p < 0.01$ vs. BLM-vehicle; # $p < 0.05$, comparing NINT 7-28 vs NINT14-28. N=5.

Micro-CT

The longitudinal micro-CT scan was performed from day 0 before any intervention till day 28. The lung aeration degree was calculated and normalized on total lung volume. All the micro-CT-derived biomarkers remained stable in saline group throughout the experiment. In the BLM-treated groups Micro-CT revealed a comparable and normal aeration in the lungs in all animals from day 0 to day 7. A reduction of normally aerated tissue in BLM+vehicle-treated group was noticed from day 7 to day 28. The NINT treatment starting from day 7 improved significantly the normo-aerated tissue at day 21 ($p<0.01$) and day 28 (58%, $p<0.01$) compared with vehicle-treated group, and NINT treatment from day 14 to 28 ameliorated the normo-aerated tissue at day 28 (47%, $p<0.01$). We did not reveal any significant differences between the two NINT-treated groups (Fig 23 A). Despite the progressive increase of hypo-aerated tissue in the BLM+vehicle-treated group, NINT ameliorated 49% of the hypo-aerated tissue in the NINT-group treated from day 7 to 28 ($p<0.05$) and 38 % in those receiving NINT from day 14 ($p<0.05$), no significant differences was found between NINT groups. The non-aerated tissue was detected from day 14 on, despite the therapeutic schedule, NINT treatment decreased significantly 66 % ($p<0.05$) of non-aerated tissue in the group treated from day 7-28 and 50% ($p<0.01$) in the nint treated group starting from day 14. The lung volume measurement by micro-CT from day 0 to 28, confirmed the augmentation of lung volume after BLM administration from day 7($p<0.01$), till day 21 in all groups compared to saline ($p<0.01$) NINT treatment regardless of the duration of therapy did not alter the lung volume, as we expected. FRC/V_{ex} was calculated for each animal. The gradual decline of this biomarker was highlighted from day 7 in all groups. NINT significantly improved FRC/V_{ex} at days 21 and 28 (62% $p<0.01$) in the group treated with NINT from day 7 and in those receiving NINT from day 14 (56%, $p<0.01$) at day 28. Even though starting the

NINT from day 7 was slightly more effective than starting from day 14, we did not obtain any statistical differences between those groups at the final timepoint.

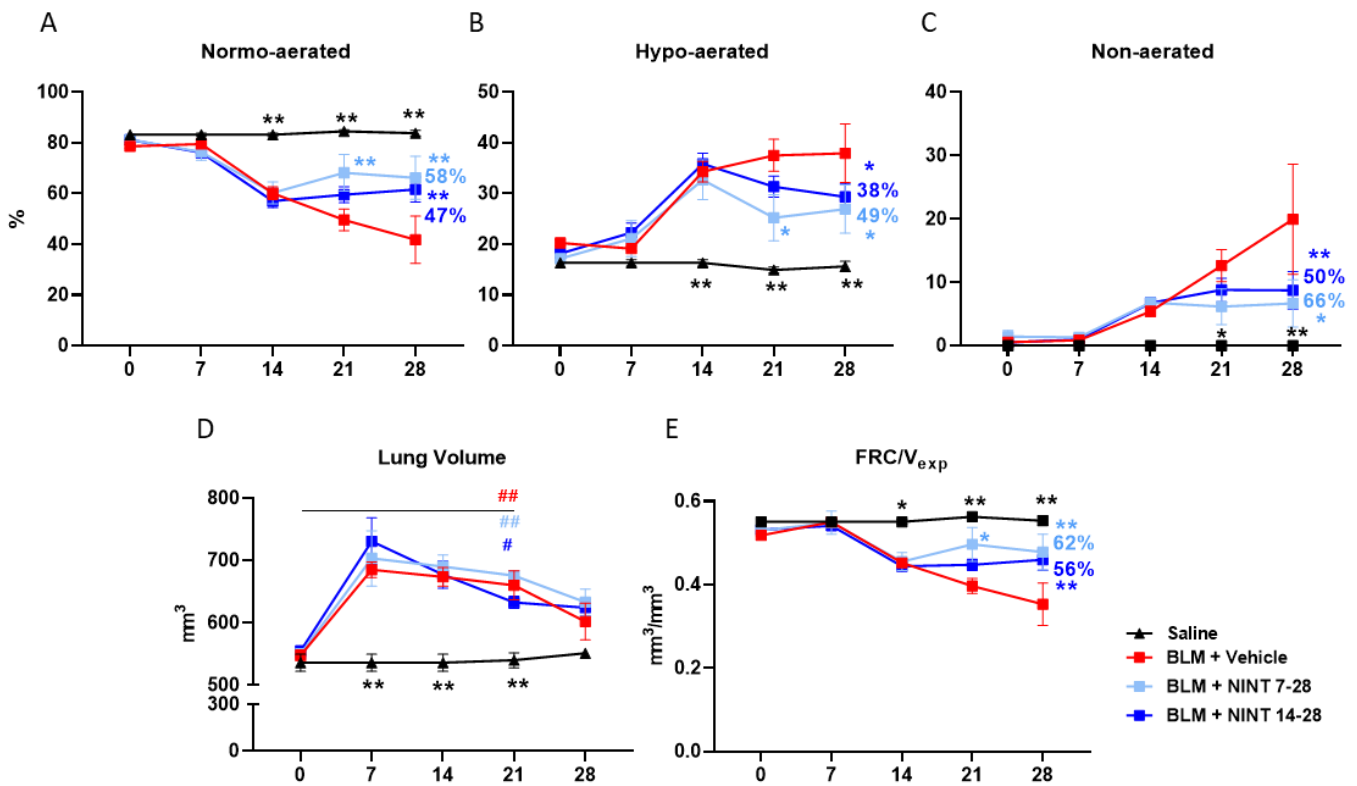


Figure 23: Longitudinal micro-CT assessment. Longitudinal lung aeration degrees expressed as percentage of normo-, hypo-, and non-aerated tissues (A, B, C), and functional parameters lung volume and FRC/V. Data are shown as mean \pm SEM (D-E) detected at 0, 7, 14, 21, 28 days for the saline group and BLM groups treated with vehicle, treated with NINT from day 7-28 and NINT from day 14-28. The statistical analysis was performed for each group compared to BLM-vehicle via two-way ANOVA followed by Dunnett's test (*p < 0.05; **p < 0.01 vs. saline). N = 5 per group.

BALF: inflammatory cells count

The inflammatory cell counts were performed in all groups at day 28. The NINT did not inhibit the total WBC counts in the BAL fluid (Fig 24A). Also, the macrophage count did not affect by NINT treatment (Fig 24B). The slight reduction of lymphocytes after two or three weeks of NINT was detected but did not reach statistical significance (Fig 24C).

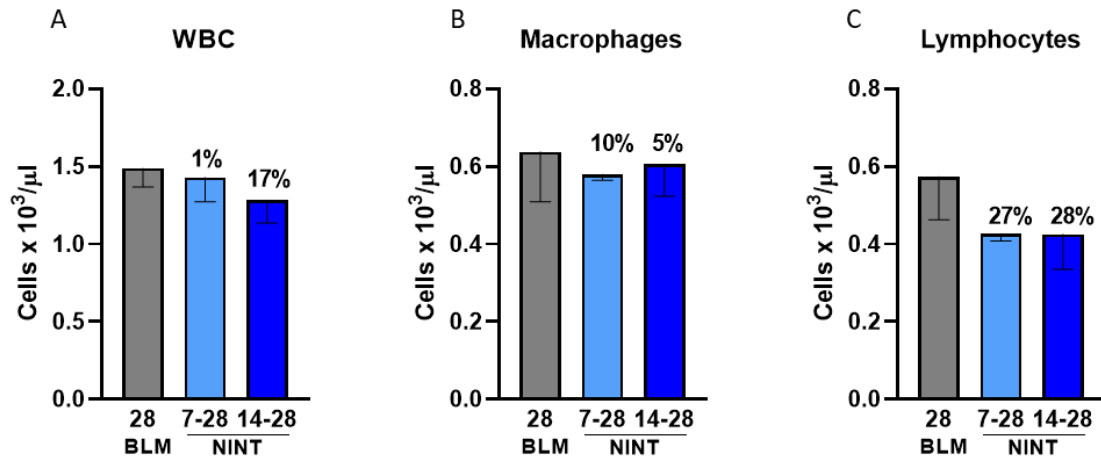


Figure 24: Inflammatory cells infiltration in BALF. Levels of total white blood cells (A), macrophages (B) and lymphocytes (C) in BALF of groups of BLM treated with vehicle, treated with NINT from day 7-28 and NINT from day 14-28. Data are shown as mean \pm SEM. The statistical analysis was performed for each group compared to BLM-vehicle via one-way ANOVA followed by Dunnett's test (* $p < 0.05$; ** $p < 0.01$ vs. saline). $N = 5$ per group.

BALF: MMPs and TIMPs quantifications

The effect of NINT on MMPs and their inhibitors between the two schemes of treatment are shown in Figure 25 A-E.

NINT from day 7 for three weeks inhibited: MMPs-2, 8 and 12 (59, 50 and 53%) and TIMP-1 and 4 (53 and 33%), on the other hand, the treatment with NINT from day 14 to 28 decreases MMPs 2-and 8 only (12 and 30%).

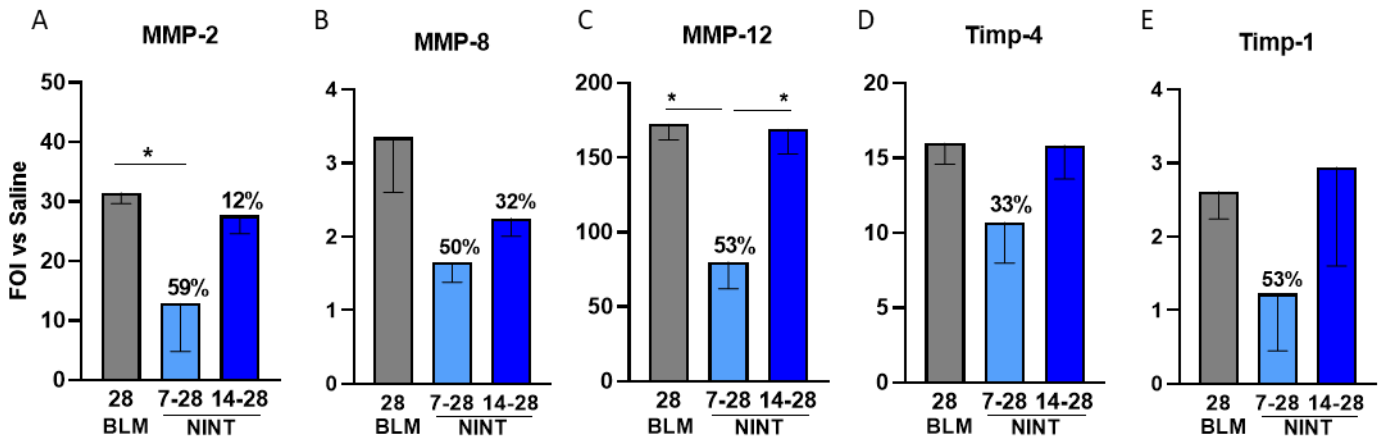


Figure 25: MMPs and TIMPs quantification in BALF. MMP-2, -8, -12 and TIMP-4, -1 (A-E in BALF from animal groups of BLM treated with vehicle, treated with NINT from day 7-28 and NINT from day 14-28. Data are shown as \pm SEM. The statistical analysis was performed for each group compared to BLM-vehicle via one-way ANOVA followed by Dunnett's test (* p <0.05; ** p <0.01 vs. saline). $N = 5$ per group.

Histological evaluation

The histological evaluation of fibrotic lungs after NINT slightly reduced the Ashcroft score at day 28 compared to vehicle treated group. The distribution of different severity of fibrotic lesions at day 28 revealed the NINT treatment ameliorated the lung parenchyma by reducing the severely injured tissue and increasing the normal tissue especially after 3 weeks of NINT treatment.(Fig 26 A-B).

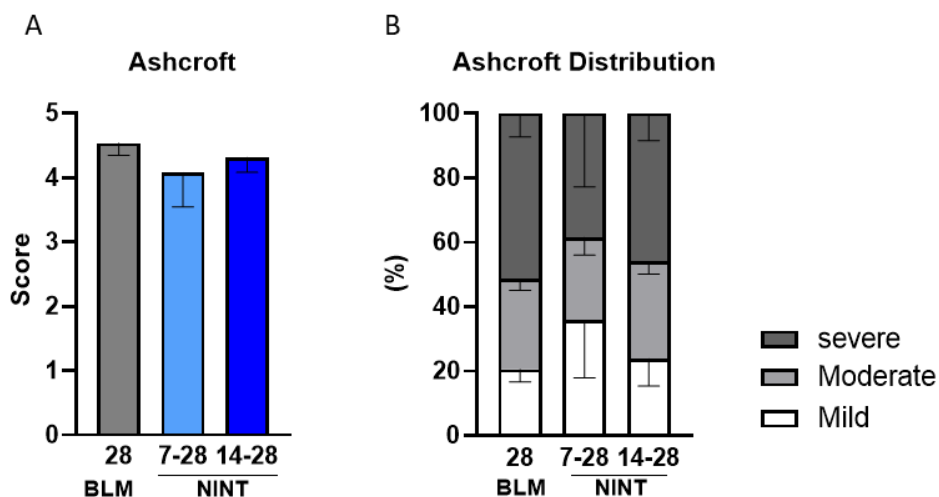


Figure 26: Histological analysis. Ashcroft score for the BLM treated with vehicle, treated with NINT from day 7-28 and NINT from day 14-28. Data are shown as \pm SEM. The statistical analysis was performed for each group compared to BLM-vehicle via one-way ANOVA followed by Dunnett's test (* p <0.05; ** p <0.01 vs. saline). $N = 5$ per group

Discussion

Animal models play a crucial role either in understanding the pathobiology of fibrosis or in drug discovery. Animals of different species, gender and age, as well as different BLM dose regimens have been used to induce lung fibrosis [21], [65], [102]–[104]. In this study, BLM dosages and the administration scheme were readjusted in male C57Bl/6 mice, as they have been reported to be more susceptible to BLM-induced fibrosis with respect to female mice [101], [104]. Thus, we tested lower BLM doses compared to those used in female mice [21] applying two different administration schemes: a double OA (10, 15 µg each) and a triple OA (5, 6 and 7.5 µg each). We hypothesized lower multiple doses of BLM might decrease acute toxicity and trigger sustained lung fibrosis for up to 28 days, thus enabling an extended time window of 3 weeks (day 7 to 28) for pharmacological intervention, guaranteeing animal welfare throughout the experiment. Micro-CT was performed longitudinally and the data were integrated with ex-vivo outcomes to select the best BLM regimen. Longitudinal imaging drastically reduced the number of mice per group and the intra-experimental variability, since the progression of the disease could be monitored in the same subjects [22], [58], [63]. All the BLM-treated groups showed decreased normo- and increased hypo-aerated tissue; however, at day 7, a significant difference with respect to the saline group in hypo-aerated tissue was revealed only in mice dosed three times with 6 µg BLM. Moreover, non-aerated regions, reflecting the most severe fibrotic lesions, were found to be dose-dependently related to BLM. This was highlighted in mice treated twice with the highest BLM dose, in contrast with those receiving the double OA at 10 µg, in which moderate fibrosis was detected. In order to assess lung fibrosis, besides considering the degrees of lung aeration, other micro-CT parameters, such as the total lung volume, the air/tissue ratio and the FRC normalized on total lung volume were proposed.

The increase of total lung volume in all BLM-treated mice at day 7 could be provoked by the acute lung inflammatory phase, associated with fluid accumulation (edema) in the lungs [105]. Overall, this increase is not related to alterations in the proportions of air or tissue volumes, as evidenced by the air/tissue ratio parameter. However, at earlier time-points multiple processes take place: a balance

between compensatory mechanisms, driven by inflammation, and collagen deposition, due to the initial stage of fibrosis, leads to an unaltered air/tissue ratio at 7 days, precluding its use to discriminate BLM group from saline. However, at later time-points, it might be a useful parameter to describe lung fibrosis progression, as well as FRC/Vexp which significantly declined at the fibrotic stage. We believe that all the micro-CT parameters need to be considered when evaluating either disease development or response to anti-fibrotic drugs. In agreement with the micro-CT data, histological analyses, depicted as the Ashcroft score and its frequency distribution, revealed that all the BLM groups developed sustained fibrosis ranging from 3.5–5. However, the Ashcroft distribution marked a dose-dependent response to BLM, as only the higher doses either in double or triple regimen, increased significantly the percentage of severely injured areas, in line with non-aerated tissue detected by micro-CT. Moreover, we found highly significant Spearman coefficients correlating the Ashcroft score with all CT parameters. A dose-dependency was also revealed in inflammatory BAL cell counts, among the groups that underwent the triple dose regimen, as the group receiving 6 µg had more prominent leukocytes infiltrate, driven mainly by lymphocytes. These data confirmed that when splitting the amount of BLM into three administrations, even slightly different amounts of BLM could result in a markedly different outcome after 28 days.

Based on our findings, the higher doses applied with both protocols, triple and double administration, were able to trigger a sustained fibrosis up to 28 days.

However, the double 15 µg BLM dose induced moderate body weight loss, histological quantification revealed a total Ashcroft score close to 5 with predominant severe fibrotic lesions. These findings, along with micro-CT outcomes, revealed a significant increase in non-aerated areas as well as a marked decrease in air/tissue ratio, which led us to consider this protocol too severe. On the other hand, the triple administration corroborated our hypothesis: both 5 and 6 µg doses were able to induce relevant changes in lung fibrosis markers detected by micro-CT and histology, without causing excessive distress and body weight loss in animals. In drug discovery, the balance between the severity of the disease model and animal welfare is crucial, as pharmacological studies require animal manipulation once or twice daily, which may cause further stress. Moreover, the evaluation

of the anti-fibrotic activity of novel compounds would require a sustained, but not excessively severe BLM-induced fibrosis. We then characterized the lung fibrosis caused by triple administration of 6 μ g of BLM till day 35 to verify the steady state of fibrosis at later timepoint. The longitudinal micro-CT data have confirmed a significant alteration in the lung densitometric parameters from day 14 to 28 showing a stable fibrotic feature with a tends to resolve at day 35. Although, the total Ashcroft score was significantly different at day 35 compared to saline, the fibrosis resulted however, moderate with a score (3.XXX).

Despite of, the frequency Ashcroft distribution displayed a reduction of moderate severe-injured tissue zones at 35 days, the severe fibrosis areas remain as observed by micro-CT analysis.

The inflammatory cells count in the BALF at days 7,14,21,28,35 revealed a significant presence of inflammatory cells till day 28.

The macrophages were found significantly higher along the study, highlighting their role either in fibrosis establishment or in the resolution phase [106], [107].

MMP-2, -8, and -12 and TIMPs are actively involved in ECM remodeling, the excessive presence of these matrixins in the BALF of the mice treated with BLM was reduced significantly after day 28, however some biomarkers like MMP-2, -12 remained still higher than saline mice till day 35 [82]. The micro-CT driven biomarkers together with ex-vivo data, confirmed an active fibrotic process till day 28 providing two-three weeks of therapeutic intervals. Although ex vivo measurements showed that some fibrosis process is still ongoing at 35 days, we decide to test Nintedaninb treatment till 28 days. The Nint was administrated following two different schemes from (7 to 28) and (14-28).

The hypo-, non- aerated and FRC/vol were introduced as a micro-CT derived biomarker to evaluate the lung fibrosis. The longitudinal quantification of these biomarkers disclosed their significant response to the antifibrotic therapy after two weeks of treatment. Based on the animal's body weight reduction, NINT was better tolerated if given for two weeks from pro-fibrotic phase (day 14) than three weeks (Fig 22). However, micro-CT driven readouts at day 28 did not reveal any significant differences between the NINT treatment starting from day 7 or day 14 , the longitudinal micro-CT

scanning highlighted an early lung aeration improvement after only one week of the treatment just in the group treated with nintedanib from day 14 (profibrotic phase); supporting the importance of timing for the pharmacological intervention[15]. The inhibitory effect of NINT on the protein levels of Matrixins and TIMPs in the BALF was found after the three weeks of treatment from day 7 to 28 which also slightly reduced the Ashcroft score and ameliorated the lung parenchyma by reducing the severely injured tissue, which was highlighted by micro-CT data.

In this study we proposed and pharmacological validate a sustained disease model of pulmonary fibrosis until day 28.

This model could be used either to study the inflammation/fibrosis, starting the therapeutic treatment for three weeks, or two weeks of treatment starting from profibrotic phase at day 14 as a therapeutic window.

The longitudinal micro-CT imaging was able to quantify the lung parenchyma changes and response to NINT along the study by reducing the intra experiment variability, since each animal was used as the control of itself. Moreover, in compliance with 3R, CT drastically reduce the number of mice needed for experiment.

Conclusion

Here, we highlighted the pivotal role of micro-CT in developing an optimized mouse model of lung fibrosis. Micro-CT technology is increasingly being recognized as a fundamental translational tool in preclinical studies, as it allows investigators to get relevant three-dimensional information about disease progression as well as to detect regional differences within the lung parenchyma. Furthermore, longitudinal measurements can be carried out from each subject in a non-invasive manner, thus enabling a significant refinement of animal studies as well as a reduction in sample size. Overall, this will permit a considerable decrease in costs and time to develop disease models. Moreover, the quantification of normo-, hypo- and non-aerated areas and functional parameters such

as air/tissue ratio and FRC/V_{exp}, provides a wide and detailed overview of the disease progression. These parameters represent useful tools to select the optimal protocol for BLM studies to be used for primary drug screening, corroborated by ex-vivo measurements. The integration of in-vivo and ex-vivo techniques provide us with broad information to outline the efficacy or toxicity of compounds in the early stage of drug discovery.

Here, we identified a triple dose of 6 µg BLM as the optimal regimen to induce sustained lung fibrosis that doesn't spontaneously revert after 21 days, and we pharmacologically validated the reliability of this model with a FDA-approved antifibrotic drug.

Bibliography

- [1] G. Raghu *et al.*, “Diagnosis of Idiopathic Pulmonary Fibrosis. An Official ATS/ERS/JRS/ALAT Clinical Practice Guideline,” <https://doi.org/10.1164/rccm.201807-1255ST>, vol. 198, no. 5, pp. e44–e68, Aug. 2018, doi: 10.1164/RCCM.201807-1255ST.
- [2] ATS and ERS, “American Thoracic Society Idiopathic Pulmonary Fibrosis : Diagnosis and Treatment,” *Am. J. Respir. Crit. Care Med.*, vol. 161, pp. 646–664, 2000, doi: 10.1164/ajrccm.161.2.ats3-00.
- [3] C. S. C. King and S. S. D. Nathan, “Idiopathic pulmonary fibrosis: effects and optimal management of comorbidities,” vol. 5, no. 1, pp. 72–84, Jan. 2017, doi: 10.1016/S2213-2600(16)30222-3.
- [4] G. Sgalla, B. Iovene, M. Calvello, M. Ori, F. Varone, and L. Richeldi, “Idiopathic pulmonary fibrosis: Pathogenesis and management,” *Respir. Res.*, vol. 19, no. 1, pp. 1–18, 2018, doi: 10.1186/s12931-018-0730-2.
- [5] G. Raghu *et al.*, “An Official ATS/ERS/JRS/ALAT Statement: Idiopathic pulmonary fibrosis: Evidence-based guidelines for diagnosis and management,” *Am. J. Respir. Crit. Care Med.*, vol. 183, no. 6, pp. 788–824, Mar. 2011, doi: 10.1164/rccm.2009-040GL.
- [6] G. Raghu, D. Weycker, J. Edelsberg, W. Z. Bradford, and G. Oster, “Incidence and Prevalence of Idiopathic Pulmonary Fibrosis,” <https://doi.org/10.1164/rccm.200602-163OC>, vol. 174, no. 7, pp. 810–816, Dec. 2012, doi: 10.1164/RCCM.200602-163OC.
- [7] J. E. Michaelson, S. M. Aguayo, and J. Roman, “Idiopathic Pulmonary Fibrosis: A Practical Approach for Diagnosis and Management,” *Chest*, vol. 118, no. 3, pp. 788–794, Sep. 2000, doi: 10.1378/CHEST.118.3.788.
- [8] K. B. Baumgartner, J. M. Samet, C. A. Stidley, T. V. Colby, and J. A. Waldron, “Cigarette smoking: a risk factor for idiopathic pulmonary fibrosis.”

<https://doi.org/10.1164/ajrccm.155.1.9001319>, vol. 155, no. 1, pp. 242–248, Dec. 2012, doi: 10.1164/AJRCCM.155.1.9001319.

- [9] T. Gustafson, A. Dahlman-Höglund, K. Nilsson, K. Ström, G. Tornling, and K. Torén, “Occupational exposure and severe pulmonary fibrosis,” *Respir. Med.*, vol. 101, no. 10, pp. 2207–2212, 2007, doi: 10.1016/j.rmed.2007.02.027.
- [10] J. P. Stewart *et al.*, “The detection of Epstein-Barr virus DNA in lung tissue from patients with idiopathic pulmonary fibrosis,” *Am. J. Respir. Crit. Care Med.*, vol. 159, no. 4 I, pp. 1336–1341, 1999, doi: 10.1164/ajrccm.159.4.9807077.
- [11] M. Jiwa, R. Steenbergen, F. Zwaan, P. Kluin, A. Raap, and M. van del Ploeg, “Three sensitive methods for the detection of cytomegalovirus in lung tissue of patients with interstitial pneumonitis,” *Am J Clin Pathol*, vol. 93, pp. 491–494, 1990.
- [12] B. B. Moore and T. A. Moore, “Viruses in idiopathic pulmonary fibrosis etiology and exacerbation,” *Ann. Am. Thorac. Soc.*, vol. 12, no. November, pp. S186–S192, 2015, doi: 10.1513/AnnalsATS.201502-088AW.
- [13] J. Le Pavec *et al.*, “Lung transplantation for idiopathic pulmonary fibrosis,” *Press. Medicale*, vol. 49, no. 2, 2020, doi: 10.1016/j.lpm.2020.104026.
- [14] J. King *et al.*, “Idiopathic Pulmonary Fibrosis: Diagnosis and Treatment,” <https://doi.org/10.1164/ajrccm.161.2.ats3-00>, vol. 161, no. 2 I, pp. 646–664, Dec. 2012, doi: 10.1164/AJRCCM.161.2.ATS3-00.
- [15] T. M. Maher and M. E. Streck, “Antifibrotic therapy for idiopathic pulmonary fibrosis: Time to treat,” *Respir. Res.*, vol. 20, no. 1, pp. 1–9, 2019, doi: 10.1186/s12931-019-1161-4.
- [16] R. Krishna, K. Chapman, and S. Ullah, “Idiopathic Pulmonary Fibrosis,” *StatPearls Publishing*, 2020. .
- [17] L. Richeldi, F. Baldi, G. Pasciuto, F. Macagno, and L. Panico, “Current and Future Idiopathic Pulmonary Fibrosis Therapy,” *Am. J. Med. Sci.*, vol. 357, no. 5, pp. 370–373, May 2019, doi:

10.1016/j.amjms.2019.02.006.

- [18] L. Wollin *et al.*, “Mode of action of nintedanib in the treatment of idiopathic pulmonary fibrosis,” *Eur. Respir. J.*, vol. 45, no. 5, pp. 1434–1445, May 2015, doi: 10.1183/09031936.00174914.
- [19] K. E. Hostettler *et al.*, “Anti-fibrotic effects of nintedanib in lung fibroblasts derived from patients with idiopathic pulmonary fibrosis,” *Respir. Res.*, vol. 15, no. 1, pp. 1–9, Dec. 2014.
- [20] L. Wollin *et al.*, “Potential of nintedanib in treatment of progressive fibrosing interstitial lung diseases,” *The European respiratory journal*, vol. 54, no. 3. NLM (Medline), 01-Sep-2019, doi: 10.1183/13993003.00161-2019.
- [21] F. Ruscitti *et al.*, “Quantification of Lung Fibrosis in IPF-Like Mouse Model and Pharmacological Response to Treatment by Micro-Computed Tomography,” *Front. Pharmacol.*, vol. 11, p. 1, Jul. 2020, doi: 10.3389/fphar.2020.01117.
- [22] F. Ravanetti *et al.*, “SSC-ILD mouse model induced by osmotic minipump delivered bleomycin: effect of Nintedanib,” *Sci. Reports 2021 111*, vol. 11, no. 1, pp. 1–10, Sep. 2021, doi: 10.1038/s41598-021-97728-z.
- [23] A. Kumar, S. Kapnadak, R. Girgis, and G. Raghu, “Lung transplantation in idiopathic pulmonary fibrosis,” *Expert Rev Respir Med*, vol. 12, no. 5, pp. 375–385, 2018, doi: 10.1080/17476348.2018.1462704.
- [24] F. Martinez *et al.*, “Idiopathic pulmonary fibrosis,” *Lancet*, vol. 389, no. 10082, pp. 1941–1952, 2017, doi: 10.1016/S0140-6736(17)30866-8.
- [25] A. L. AL Degryse and W. W. E. Lawson, “Progress toward improving animal models for idiopathic pulmonary fibrosis,” in *American Journal of the Medical Sciences*, 2011, vol. 341, no. 6, pp. 444–449, doi: 10.1097/MAJ.0b013e31821aa000.
- [26] R. G. Jenkins *et al.*, “An Official American Thoracic Society Workshop Report: Use of Animal Models for the Preclinical Assessment of Potential Therapies for Pulmonary

Fibrosis,” <https://doi.org/10.1165/rcmb.2017-0096ST>, vol. 56, no. 5, pp. 667–679, May 2017, doi: 10.1165/RCMB.2017-0096ST.

- [27] B. B. Moore and C. M. Hogaboam, *Murine models of pulmonary fibrosis*, vol. 294, no. 2. American Physiological Society, 2008, pp. 152–160.
- [28] N. Geifman and E. Rubin, “The mouse age phenome knowledgebase and disease-specific inter-species age mapping,” *PLoS One*, vol. 8, no. 12, 2013, doi: 10.1371/journal.pone.0081114.
- [29] H. Jin, Y. Yoo, Y. Kim, Y. Kim, J. Cho, and Y.-S. Lee, “Radiation-Induced Lung Fibrosis: Preclinical Animal Models and Therapeutic Strategies.,” *Cancers (Basel)*, vol. 12, no. 6, pp. 1–24, Jun. 2020, doi: 10.3390/cancers12061561.
- [30] T. Miles, G. F. Hoyne, D. A. Knight, M. W. Fear, S. E. Mutsaers, and C. M. Prêle, “The contribution of animal models to understanding the role of the immune system in human idiopathic pulmonary fibrosis,” *Clin. Transl. Immunol.*, vol. 9, no. 7, pp. 1–14, 2020, doi: 10.1002/cti2.1153.
- [31] Z. Debyser, “Biosafety of lentiviral vectors,” *Curr. Gene Ther.*, vol. 3, no. 6, pp. 517–525, 2003, doi: 10.2174/1566523034578177.
- [32] P. J. Sime, Z. Xing, F. L. Graham, K. G. Csaky, and J. Gauldie, “Adenovector-mediated gene transfer of active transforming growth factor- β 1 induces prolonged severe fibrosis in rat lung,” *J. Clin. Invest.*, vol. 100, no. 4, pp. 768–776, 1997, doi: 10.1172/JCI119590.
- [33] M.-E. E. Bergeron, A. Stefanov, C. K. Haston, B. ME, S. A, and H. CK, “Fine mapping of the major bleomycin-induced pulmonary fibrosis susceptibility locus in mice,” *Mamm. Genome*, vol. 29, no. 9–10, pp. 670–679, Oct. 2018, doi: 10.1007/S00335-018-9774-3.
- [34] V. Roggli *et al.*, “Pathology of Asbestosis: An Update of the Diagnostic Criteria Response to a Critique,” *Arch. Pathol. Lab. Med.*, vol. 140, no. 9, pp. 950–952, Sep. 2016, doi: 10.5858/ARPA.2015-0503-SA.

- [35] J. Li, H. G. Poovey, J. F. Rodriguez, A. R. Brody, and G. W. Hoyle, "Effect of Platelet-Derived Growth Factor on the Development and Persistence of Asbestos-Induced Fibroproliferative Lung Disease," *J. Environ. Pathol. Toxicol. Oncol.*, vol. 23, no. 4, pp. 253–266, 2004, doi: 10.1615/JENVPATHTOXONCOL.V23.I4.20.
- [36] B. B. Moore, W. E. Lawson, T. D. Oury, T. H. Sisson, K. Raghavendran, and C. M. Hogaboam, "Animal models of fibrotic lung disease," *Am. J. Respir. Cell Mol. Biol.*, vol. 49, no. 2, pp. 167–179, Aug. 2013, doi: 10.1165/rcmb.2013-0094TR.
- [37] J. M. Englert *et al.*, "A Role for the Receptor for Advanced Glycation End Products in Idiopathic Pulmonary Fibrosis," *Am. J. Pathol.*, vol. 172, no. 3, pp. 583–591, Mar. 2008, doi: 10.2353/AJPATH.2008.070569.
- [38] C. S. Samuel *et al.*, "Relaxin deficiency in mice is associated with an age-related progression of pulmonary fibrosis.," *FASEB J.*, vol. 17, no. 1, pp. 121–123, 2003, doi: 10.1096/FJ.02-0449FJE.
- [39] Y. Lin and Z. Xu, "Fibroblast Senescence in Idiopathic Pulmonary Fibrosis," *Front. Cell Dev. Biol.*, vol. 8, p. 1398, Nov. 2020, doi: 10.3389/FCELL.2020.593283/XML/NLM.
- [40] Y. Y. Sanders, P. Kumbala, and J. S. Hagood, "Enhanced Myofibroblastic Differentiation and Survival in Thy-1(-) Lung Fibroblasts," <https://doi.org/10.1165/rcmb.2006-0178OC>, vol. 36, no. 2, pp. 226–235, Dec. 2012, doi: 10.1165/RCMB.2006-0178OC.
- [41] A. F. Muro *et al.*, "An Essential Role for Fibronectin Extra Type III Domain A in Pulmonary Fibrosis," *Am. J. Respir. Crit. Care Med.*, vol. 177, no. 6, p. 638, Mar. 2008, doi: 10.1164/RCCM.200708-1291OC.
- [42] C. G. Lee *et al.*, "Early Growth Response Gene 1-mediated Apoptosis Is Essential for Transforming Growth Factor β 1-induced Pulmonary Fibrosis," *J. Exp. Med.*, vol. 200, no. 3, p. 377, Aug. 2004, doi: 10.1084/JEM.20040104.
- [43] Chun Geun Lee *et al.*, "Interleukin-13 Induces Tissue Fibrosis by Selectively Stimulating and

Activating Transforming Growth Factor β 1,” *J. Exp. Med.*, vol. 194, no. 6, p. 809, Sep. 2001, doi: 10.1084/JEM.194.6.809.

- [44] P. J. Sime *et al.*, “Transfer of Tumor Necrosis Factor- α to Rat Lung Induces Severe Pulmonary Inflammation and Patchy Interstitial Fibrogenesis with Induction of Transforming Growth Factor- β 1 and Myofibroblasts,” *Am. J. Pathol.*, vol. 153, no. 3, pp. 825–832, Sep. 1998, doi: 10.1016/S0002-9440(10)65624-6.
- [45] E. Exhibit *et al.*, “Amiodarone Pulmonary Toxicity : Pictorial Review of the Main Radiological Manifestations,” 2017.
- [46] P. G. Reinhart and C. G. Gairola, “Amiodarone-induced pulmonary toxicity in Fischer rats: release of tumor necrosis factor alpha and transforming growth factor beta by pulmonary alveolar macrophages.,” *J. Toxicol. Environ. Health*, vol. 52, no. 4, pp. 353–65, Nov. 1997, doi: 10.1080/00984109708984070.
- [47] P. Mahavadi *et al.*, “Altered surfactant homeostasis and alveolar epithelial cell stress in amiodarone-induced lung fibrosis,” *Toxicol. Sci.*, vol. 142, no. 1, pp. 285–297, 2014, doi: 10.1093/toxsci/kfu177.
- [48] Y. Futamura, “Amiodarone induces two different types of disorders in mouse alveolar macrophages,” *Jpn. J. Pharmacol.*, vol. 74, no. 1, pp. 21–28, 1997, doi: 10.1254/jjp.74.21.
- [49] F. C. Roth, J. E. Mulder, J. F. Brien, T. Takahashi, and T. E. Massey, “Cytotoxic interaction between amiodarone and desethylamiodarone in human peripheral lung epithelial cells,” *Chem. Biol. Interact.*, vol. 204, no. 3, pp. 135–139, 2013, doi: 10.1016/j.cbi.2013.05.006.
- [50] C. H. Niu, Y. Wang, J. Di Liu, J. L. Wang, and J. H. Xiao, “Protective effects of neferine on amiodarone-induced pulmonary fibrosis in mice,” *Eur. J. Pharmacol.*, vol. 714, no. 1–3, pp. 112–119, 2013, doi: 10.1016/j.ejphar.2013.06.004.
- [51] Z. Yu *et al.*, “Targeted Delivery of Bleomycin: A Comprehensive Anticancer Review,” *Curr. Cancer Drug Targets*, vol. 16, no. 6, pp. 509–521, 2016, doi:

10.2174/1568009616666151130213910.

- [52] V. Della Latta, A. Cecchetti, S. Del Ry, and M. A. Morales, "Bleomycin in the setting of lung fibrosis induction: From biological mechanisms to counteractions," *Pharmacological Research*, vol. 97. Academic Press, pp. 122–130, 02-Jun-2015, doi: 10.1016/j.phrs.2015.04.012.
- [53] E. Azambuja, J. F. Fleck, R. G. Batista, and S. S. Menna Barreto, "Bleomycin lung toxicity: Who are the patients with increased risk?," *Pulm. Pharmacol. Ther.*, vol. 18, no. 5, pp. 363–366, Oct. 2005, doi: 10.1016/J.PUPT.2005.01.007.
- [54] J. Tashiro *et al.*, "Exploring Animal Models That Resemble Idiopathic Pulmonary Fibrosis," *Front. Med.*, vol. 4, no. JUL, p. 118, 2017, doi: 10.3389/FMED.2017.00118.
- [55] J. William Lown and S. K. Sim, "The mechanism of the bleomycin-induced cleavage of DNA," *Biochem. Biophys. Res. Commun.*, vol. 77, no. 4, pp. 1150–1157, Aug. 1977, doi: 10.1016/S0006-291X(77)80099-5.
- [56] T. Liu *et al.*, "Telomerase activity is required for bleomycin-induced pulmonary fibrosis in mice," *J. Clin. Invest.*, vol. 117, no. 12, p. 3800, Dec. 2007, doi: 10.1172/JCI32369.
- [57] F. Ravanetti *et al.*, "Modeling pulmonary fibrosis through bleomycin delivered by osmotic minipump: a new histomorphometric method of evaluation," *Am J Physiol Cell Mol Physiol*, vol. 318, no. 2, pp. L376–L385, Feb. 2020, doi: 10.1152/ajplung.00311.2019.
- [58] F. E *et al.*, "Alfaxalone and Dexmedetomidine as an Alternative to Gas Anesthesia for Micro-CT Lung Imaging in a Bleomycin-Induced Pulmonary Fibrosis Murine Model," p. 759, Oct. 2020, doi: 10.3389/FVETS.2020.588592.
- [59] M. A. Mouratis and V. Aidinis, *Modeling pulmonary fibrosis with bleomycin*, vol. 17, no. 5. Curr Opin Pulm Med, 2011, pp. 355–361.
- [60] C. K. Haston *et al.*, "Bleomycin hydrolase and a genetic locus within the MHC affect risk for pulmonary fibrosis in mice," vol. 11, no. 16, pp. 1855–1863, Aug. 2002, doi:

10.1093/HMG/11.16.1855.

- [61] E. F. Redente *et al.*, "Age and sex dimorphisms contribute to the severity of bleomycin-induced lung injury and fibrosis," *Am. J. Physiol. - Lung Cell. Mol. Physiol.*, vol. 301, no. 4, p. L510, Oct. 2011, doi: 10.1152/AJPLUNG.00122.2011.
- [62] L. Mecozzi *et al.*, "In-vivo lung fibrosis staging in a bleomycin-mouse model: a new micro-CT guided densitometric approach," *Sci. Rep.*, vol. 10, no. 1, Dec. 2020, doi: 10.1038/s41598-020-71293-3.
- [63] F. Ruscitti *et al.*, "Longitudinal assessment of bleomycin-induced lung fibrosis by Micro-CT correlates with histological evaluation in mice," *Multidiscip. Respir. Med.*, vol. 12, no. 1, pp. 1–10, Apr. 2017, doi: 10.1186/s40248-017-0089-0.
- [64] N. I. Chaudhary, A. Schnapp, and J. E. Park, "Pharmacologic differentiation of inflammation and fibrosis in the rat bleomycin model," *Am. J. Respir. Crit. Care Med.*, vol. 173, no. 7, pp. 769–776, Apr. 2006, doi: 10.1164/RCCM.200505-717OC.
- [65] T. Yanagihara, S. G. Chong, M. Vierhout, J. A. Hirota, K. Ask, and M. Kolb, "Current models of pulmonary fibrosis for future drug discovery efforts," <https://doi.org/10.1080/17460441.2020.1755252>, vol. 15, no. 8, pp. 931–941, Aug. 2020, doi: 10.1080/17460441.2020.1755252.
- [66] J. K. Park *et al.*, "Bleomycin Induces Drug Efflux in Lungs. A Pitfall for Pharmacological Studies of Pulmonary Fibrosis," *Am. J. Respir. Cell Mol. Biol.*, vol. 62, no. 2, pp. 178–190, 2020, doi: 10.1165/RCMB.2018-0147OC.
- [67] P. Kolb *et al.*, "The importance of interventional timing in the bleomycin model of pulmonary fibrosis," *Eur. Respir. J.*, vol. 55, no. 6, Jun. 2020, doi: 10.1183/13993003.01105-2019.
- [68] N. Inui, S. Sakai, and M. Kitagawa, "Molecular Pathogenesis of Pulmonary Fibrosis, with Focus on Pathways Related to TGF- β and the Ubiquitin-Proteasome Pathway," *Int J Mol Sci*, vol. 22, no. 11, 2021, doi: 10.3390/ijms22116107.

- [69] A. V. Samarelli *et al.*, “Dissecting the Role of Mesenchymal Stem Cells in Idiopathic Pulmonary Fibrosis: Cause or Solution,” *Front. Pharmacol.*, vol. 12, no. July, pp. 1–21, 2021, doi: 10.3389/fphar.2021.692551.
- [70] N. Sandbo, “Mechanisms of Fibrosis in IPF,” in *Idiopathic Pulmonary Fibrosis: A Comprehensive Clinical Guide*, New York: Respiratory Medicine, 2014, pp. 161–187.
- [71] M. Aspal and R. L. Zemans, “Mechanisms of ATII-to-ATI cell differentiation during lung regeneration,” *Int. J. Mol. Sci.*, vol. 21, no. 9, 2020, doi: 10.3390/ijms21093188.
- [72] M. Selman and A. Pardo, “Role of epithelial cells in idiopathic pulmonary fibrosis: from innocent targets to serial killers,” *Proc Am Thorac Soc*, vol. 3, no. 4, pp. 364–372, 2006, doi: 10.1513/pats.200601-003TK.
- [73] F. Salton, M. C. Volpe, and M. Confalonieri, “Epithelial-mesenchymal transition in the pathogenesis of idiopathic pulmonary fibrosis,” *Med.*, vol. 55, no. 4, pp. 1–8, 2019, doi: 10.3390/medicina55040083.
- [74] V. Thannickal and J. Horowitz, “Evolving concepts of apoptosis in idiopathic pulmonary fibrosis,” *Proc. Am. Thorac. Soc.*, vol. 3, no. 6A, pp. 350–356, 2006, doi: 10.1513/pats.200601-001TK.
- [75] W. A. Wuyts *et al.*, “The pathogenesis of pulmonary fibrosis: A moving target,” *Eur. Respir. J.*, vol. 41, no. 5, pp. 1207–1218, 2013, doi: 10.1183/09031936.00073012.
- [76] T. Parimon, C. Yao, B. R. Stripp, P. W. Noble, and P. Chen, “Alveolar epithelial type II cells as drivers of lung fibrosis in idiopathic pulmonary fibrosis,” *Int. J. Mol. Sci.*, vol. 21, no. 7, 2020, doi: 10.3390/ijms21072269.
- [77] M. Yilmaz and G. Christofori, “EMT, the cytoskeleton, and cancer cell invasion,” *Cancer Metastasis Rev.*, vol. 28, no. 1–2, pp. 15–33, 2009, doi: 10.1007/s10555-008-9169-0.
- [78] R. T. Kendall and C. A. Feghali-Bostwick, “Fibroblasts in fibrosis: Novel roles and mediators,” *Front. Pharmacol.*, vol. 5, no. 123, pp. 1–13, 2014, doi:

10.3389/fphar.2014.00123.

- [79] G. Bagnato and S. Harari, "Cellular interactions in the pathogenesis of interstitial lung diseases," *Eur. Respir. Rev.*, vol. 24, no. 135, pp. 102–114, 2015, doi: 10.1183/09059180.00003214.
- [80] N. Enomoto *et al.*, "Quantitative analysis of fibroblastic foci in usual interstitial pneumonia," *Chest*, vol. 130, no. 1, pp. 22–29, 2006, doi: 10.1378/chest.130.1.22.
- [81] M. E. Blaauboer *et al.*, "Extracellular matrix proteins: A positive feedback loop in lung fibrosis?," *Matrix Biol.*, vol. 34, pp. 170–178, 2014, doi: 10.1016/j.matbio.2013.11.002.
- [82] A. Pardo, S. Cabrera, M. Maldonado, and M. Selman, "Role of matrix metalloproteinases in the pathogenesis of idiopathic pulmonary fibrosis," *Respir. Res.*, vol. 17, no. 1, Mar. 2016, doi: 10.1186/S12931-016-0343-6.
- [83] V. J. Craig, L. Zhang, J. S. Hagood, and C. A. Owen, "Matrix metalloproteinases as therapeutic targets for idiopathic pulmonary fibrosis," *Am. J. Respir. Cell Mol. Biol.*, vol. 53, no. 5, pp. 585–600, Nov. 2015, doi: 10.1165/RCMB.2015-0020TR/SUPPL_FILE/DISCLOSURES.PDF.
- [84] A. Pardo, M. Selman, and N. Kaminski, "Approaching the degradome in idiopathic pulmonary fibrosis," *Int. J. Biochem. Cell Biol.*, vol. 40, no. 6–7, pp. 1141–1155, Jun. 2008, doi: 10.1016/J.BIOCEL.2007.11.020.
- [85] T. Bormann *et al.*, "Role of matrix metalloprotease-2 and MMP-9 in experimental lung fibrosis in mice," vol. 23, no. 1, pp. 1–12, 2022.
- [86] E. García-Prieto *et al.*, "Resistance to Bleomycin-Induced Lung Fibrosis in MMP-8 Deficient Mice Is Mediated by Interleukin-10," *PLoS One*, vol. 5, no. 10, p. e13242, 2010, doi: 10.1371/JOURNAL.PONE.0013242.
- [87] M. Cedilak *et al.*, "Precision-cut lung slices from bleomycin treated animals as a model for testing potential therapies for idiopathic pulmonary fibrosis," *Pulm. Pharmacol. Ther.*, vol.

55, pp. 75–83, Apr. 2019, doi: 10.1016/j.pupt.2019.02.005.

- [88] G. Matute-Bello *et al.*, “Essential role of MMP-12 in Fas-induced lung fibrosis,” *Am. J. Respir. Cell Mol. Biol.*, vol. 37, no. 2, pp. 210–221, Aug. 2007, doi: 10.1165/RCMB.2006-0471OC.
- [89] M. Selman *et al.*, “TIMP-1, -2, -3, and -4 in idiopathic pulmonary fibrosis. A prevailing nondegradative lung microenvironment?,” *Am. J. Physiol. - Lung Cell. Mol. Physiol.*, vol. 279, no. 3 23-3, 2000, doi: 10.1152/AJPLUNG.2000.279.3.L562/ASSET/IMAGES/LARGE/H50900065010.JPEG.
- [90] V. Ruiz *et al.*, “Unbalanced collagenases/TIMIP-1 expression and epithelial apoptosis in experimental lung fibrosis,” *Am. J. Physiol. - Lung Cell. Mol. Physiol.*, vol. 285, no. 5 29-5, pp. 1026–1036, 2003, doi: 10.1152/AJPLUNG.00183.2003/ASSET/IMAGES/LARGE/H51131540008.JPEG.
- [91] S. S. V. P. Sakamuri *et al.*, “Absence of Tissue Inhibitor of Metalloproteinase-4 (TIMP4) ameliorates high fat diet-induced obesity in mice due to defective lipid absorption,” *Sci. Reports 2017 71*, vol. 7, no. 1, pp. 1–13, Jul. 2017, doi: 10.1038/s41598-017-05951-4.
- [92] J. Tannenbaum and B. T. Bennett, “Russell and Burch’s 3Rs then and now: The need for clarity in definition and purpose,” *J. Am. Assoc. Lab. Anim. Sci.*, vol. 54, no. 2, pp. 120–132, 2015.
- [93] D. P. Clark and C. T. Badea, “Micro-CT of rodents: State-of-the-art and future perspectives,” *Physica Medica*, vol. 30, no. 6. Associazione Italiana di Fisica Medica, pp. 619–634, 2014, doi: 10.1016/j.ejmp.2014.05.011.
- [94] P. Russo and C. T. Badea, “Small Animal X-ray Computed Tomography,” *Handb. X-ray Imaging*, no. 749, pp. 749–773, 2019, doi: 10.1201/9781351228251-36.
- [95] E. Ferrini *et al.*, “A new anesthesia protocol enabling longitudinal lung function measurements in neonatal rabbits by micro-CT,” *Am J Physiol Lung Cell Mol Physiol*, 2021,

doi: 10.1152/ajplung.00328.2021.

- [96] S. J. Blocker, M. D. Holbrook, Y. M. Mowery, D. C. Sullivan, and C. T. Badea, "The impact of respiratory gating on improving volume measurement of murine lung tumors in micro-CT imaging," *PLoS One*, vol. 15, no. 2, p. e0225019, 2020, doi: 10.1371/JOURNAL.PONE.0225019.
- [97] Z. Khalajzeyqami *et al.*, "Pivotal role of micro-CT technology in setting up an optimized lung fibrosis mouse model for drug screening," *PLoS One*, vol. 17, no. 6, p. e0270005, Jun. 2022, doi: 10.1371/JOURNAL.PONE.0270005.
- [98] L. Gattinoni, P. Caironi, P. Pelosi, and L. R. Goodman, "What has computed tomography taught us about the acute respiratory distress syndrome?," *Am. J. Respir. Crit. Care Med.*, vol. 164, no. 9, pp. 1701–1711, 2001, doi: 10.1164/ajrccm.164.9.2103121.
- [99] E. Morgan *et al.*, "Cytometric bead array: A multiplexed assay platform with applications in various areas of biology," *Clin. Immunol.*, vol. 110, no. 3, pp. 252–266, 2004, doi: 10.1016/j.clim.2003.11.017.
- [100] R. H. Hübner *et al.*, "Standardized quantification of pulmonary fibrosis in histological samples," *Biotechniques*, vol. 44, no. 4, pp. 507–11, 514–7, 2008, doi: 10.2144/000112729.
- [101] F. F. Stellari *et al.*, "Heterologous Matrix Metalloproteinase Gene Promoter Activity Allows In Vivo Real-time Imaging of Bleomycin-Induced Lung Fibrosis in Transiently Transgenized Mice," *Front. Immunol.*, no. MAR, p. 199, Mar. 2017.
- [102] D. M. Walters and S. R. Kleeberger, "Mouse Models of Bleomycin-Induced Pulmonary Fibrosis," *Curr. Protoc. Pharmacol.*, vol. 40, no. 1, pp. 5.46.1-5.46.17, Mar. 2008, doi: 10.1002/0471141755.PH0546S40.
- [103] N. C. Henderson, F. Rieder, and T. A. Wynn, "Fibrosis: from mechanisms to medicines," *Nat. 2020 5877835*, vol. 587, no. 7835, pp. 555–566, Nov. 2020, doi: 10.1038/s41586-020-2938-9.

- [104] D. G. Hoyt and J. S. Lazo, "Alterations in pulmonary mRNA encoding procollagens, fibronectin and transforming growth factor-beta precede bleomycin-induced pulmonary fibrosis in mice.," *J. Pharmacol. Exp. Ther.*, vol. 246, no. 2, 1988.
- [105] G. Vande Velde *et al.*, "Longitudinal micro-CT provides biomarkers of lung disease that can be used to assess the effect of therapy in preclinical mouse models, and reveal compensatory changes in lung volume," *DMM Dis. Model. Mech.*, vol. 9, no. 1, pp. 91–98, Jan. 2016, doi: 10.1242/dmm.020321.
- [106] L. Zhang, Y. Wang, G. Wu, W. Xiong, W. Gu, and C. Y. Wang, "Macrophages: friend or foe in idiopathic pulmonary fibrosis?," *Respir. Res.*, vol. 19, no. 1, Sep. 2018, doi: 10.1186/S12931-018-0864-2.
- [107] P. Cheng, S. Li, and H. Chen, "Macrophages in Lung Injury, Repair, and Fibrosis," *Cells*, vol. 10, no. 2, pp. 1–17, Feb. 2021, doi: 10.3390/CELLS10020436.